



Article

Monitoring and Quantifying Soil Erosion and Sedimentation Rates in Centimeter Accuracy Using UAV-Photogrammetry, GNSS, and t-LiDAR in a Post-Fire Setting

Simoni Alexiou ^{1,2}, Ioannis Papanikolaou ^{1,*} , Sascha Schneiderwind ³, Valerie Kehrle ³ and Klaus Reicherter ³

¹ Laboratory of Mineralogy and Geology, Department of Natural Resources & Agricultural Engineering, Agricultural University of Athens, 75 Iera Odos Str., 11855 Athens, Greece; sim.alexiou@aua.gr

² Department of Tactical Operation Informatics and Geospatial Analysis, Division of Informatics and Telecommunications, Hellenic Fire Brigade, 18346 Athens, Greece

³ Institute of Neotectonics and Natural Hazards, RWTH Aachen University, 52062 Aachen, Germany; s.schneiderwind@nug.rwth-aachen.de (S.S.); k.reicherter@nug.rwth-aachen.de (K.R.)

* Correspondence: i.pap@aua.gr

Abstract: Remote sensing techniques, namely Unmanned Aerial Vehicle (UAV) photogrammetry and t-LiDAR (terrestrial Light Detection and Ranging), two well-established techniques, were applied for seven years in a mountainous Mediterranean catchment in Greece (Ilioupoli test site, Athens), following a wildfire event in 2015. The goal was to monitor and quantify soil erosion and sedimentation rates with cm accuracy. As the frequency of wildfires in the Mediterranean has increased, this study aims to present a methodological approach for monitoring and quantifying soil erosion and sedimentation rates in post-fire conditions, through high spatial resolution field measurements acquired using a UAV survey and a t-LiDAR (or TLS—Terrestrial Laser Scanning), in combination with georadar profiles (Ground Penetration Radar—GPR) and GNSS. This test site revealed that 40 m³ of sediment was deposited following the first intense autumn rainfall events, a value that was decreased by 50% over the next six months (20 m³). The UAV-SfM technique revealed only 2 m³ of sediment deposition during the 2018–2019 analysis, highlighting the decrease in soil erosion rates three years after the wildfire event. In the following years (2017–2021), erosion and sedimentation decreased further, confirming the theoretical pattern, whereas sedimentation over the first year after the fire was very high and then sharply lessened as vegetation regenerated. The methodology proposed in this research can serve as a valuable guide for achieving high-precision sediment yield deposition measurements based on a detailed analysis of 3D modeling and a point cloud comparison, specifically leveraging the dense data collection facilitated by UAV-SfM and TLS technology. The resulting point clouds effectively replicate the fine details of the topsoil microtopography within the upland dam basin, as highlighted by the profile analysis. Overall, this research clearly demonstrates that after monitoring the upland area in post-fire conditions, the UAV-SfM method and LiDAR cm-scale data offer a realistic assessment of the retention dam's life expectancy and management planning. These observations are especially crucial for assessing the impacts in the wildfire-affected areas, the implementation of mitigation strategies, and the construction and maintenance of retention dams.

Keywords: soil erosion; geoenvironment; point cloud; remote sensing; structure from motion; TLS; GNSS



Citation: Alexiou, S.; Papanikolaou, I.; Schneiderwind, S.; Kehrle, V.; Reicherter, K. Monitoring and Quantifying Soil Erosion and Sedimentation Rates in Centimeter Accuracy Using UAV-Photogrammetry, GNSS, and t-LiDAR in a Post-Fire Setting. *Remote Sens.* **2024**, *16*, 802. <https://doi.org/10.3390/rs16050802>

Academic Editors: Francesca Ardizzone, Gabriella Caroti and Yuankun Xu

Received: 20 January 2024

Revised: 17 February 2024

Accepted: 22 February 2024

Published: 25 February 2024



Copyright: © 2024 by the authors. Licensee MDPI, Basel, Switzerland. This article is an open access article distributed under the terms and conditions of the Creative Commons Attribution (CC BY) license (<https://creativecommons.org/licenses/by/4.0/>).

1. Introduction

Soil erosion, a natural process that degrades soil, primarily results from the physical forces of water and wind impacting exposed soil surfaces, making it a significant contributor to soil degradation [1]. Mediterranean mountainous regions exhibit substantial spatial and temporal fluctuations in vegetation cover [2], often correlated with significant alterations in land usage and topography. These changes have a direct impact both on water resources and the

susceptibility to either soil erosion or conservation. Experimental plots and watersheds have led to both soil erosion parameter clarification and dynamic process analysis in correlation with the sediment fluxes [3–5].

Human interventions geomorphologically alter the environment, surpassing the geological sediment yielding [6,7]. As [8] argued, since the early 1960s, the frequency of wildfires in the Mediterranean due to land-use change and rural development, correlated to the weather conditions, has increased. While infrequent, mega-fires that have occurred frequently over recent decades, in exceptionally dry and windy conditions, can have devastating consequences on infrastructure, the environment, and human lives, leading to extensive costs for suppression and rehabilitation. Beyond the immediate aftermath, these fires also trigger lasting impacts on geomorphological and hydrological processes, which, in turn, influence environmental conditions and may contribute to the occurrence of natural hazards like floods and mass movements [9]. Following a wildfire event, the number of plant species tremendously decreases. Apart from vegetation removal, wildfires cause a severe topsoil SOM (soil organic matter) depletion, affecting soil texture, soil permeability, nutrients, and leading to soil chemical alteration. The spatial–temporal differentiation of these parameters is correlated to wildfire severity, topography, ecosystem recovery, and weather conditions [10,11].

Post-fire erosion is a critical field of study that focuses on understanding and mitigating the heightened erosion risks in areas affected by wildfires. Indeed, it is evident that alterations in vegetation structure and community composition, especially in the aftermath of recurrent fires, can have profound effects on erosional processes and the overall recovery of ecosystems [12]. Significant results in [13] highlighted the forest recovery period to be 5–10 years. Early research showed that the greatest erosion and runoff rates are recorded within the first 1–2 years following the fire event, while the soil erosion values depend on the fire intensity, fire characteristics [14], and climatic characteristics [15,16]. Additional research [17,18] showed that for the hillslope sediment yield balance, three to five years are required.

Soil erosion rate and sediment yield estimation contribute to proper soil management practices, indicating areas prone to high, moderate, and low soil degradation risk. Understanding soil erosion processes is important for geomorphological analysis and erosion rate prediction [9,19,20]. The difference between on-site and off-site erosion impact should be denoted. On-site erosion is attributed to soil loss and fertility loss due to a soil organic matter decrease, resulting in a reduced vegetation cover [21]. Off-site erosion corresponds to floods and a reservoir lifetime decline [22]. Reservoirs act like sediment traps for the wider watershed, where the sediment processes control the yield, resulting in continuous sedimentary sequences susceptible to land-use change and human activity [23]. Check dams represent a widely employed technique for mitigating erosion hazards, as supported by several studies [24–27]. These structures effectively capture sediments from upland areas and reduce the flow velocity of water, thereby leading to a reduction in the amount of sediment entering downstream channels [28].

Soil erosion analysis, in terms of the multi-temporal t-LiDAR survey approach, has been conducted over the last 12 years [29–31], investigating different soil erosion processes such as rill erosion analysis [32–35] or gully erosion [35–41]. The t-LiDAR approach led us to develop new methods such as point cloud (PC) analysis and multiscale 3D model production [42–46], resulting in high-resolution geometric models and 3D surface reconstruction.

There has been a surge of interest in the Unmanned Aerial Vehicle (UAV) Structure from Motion (SfM) data collection technique, primarily driven by the cost-effectiveness of the equipment and the enhanced speed of data acquisition. This method, combined with recent advancements in computer technology, has positioned photogrammetry as a robust tool for geomorphological research [47]. Applications across various domains, such as monitoring riverbed topography [48–51], riverbank analysis [52,53], erosion [38,54–57], landslides [58], erosion rate assessment [59–64], coastal analysis [65], and rockfall/rock slope stability analysis [66], have significantly expanded the realm of geomorphological analysis. In the past five years, there has been a notable interest in point cloud analysis based on the 3D surface reconstruction of infrastructure or natural surfaces [67–72]. Recent research [73]

has contributed by quantifying the changes in surface topography through the generation of a time series of point clouds. This is achieved by creating multiple terrain models and orthomosaics using SfM photogrammetric techniques. The digital comparison of these co-registered photogrammetric products has unveiled noteworthy topsoil variations.

The GNSS (Global Navigation Satellite System) defines the coordinates of reference ground control points (GCPs) within a worldwide reference system. Various GNSS positioning methods can be utilized depending on factors such as the desired accuracy, the availability of receivers, real-time coordinate requirements, and the frequency of survey repetitions [74,75]. Access to the area of interest is essential and the proper marking of target points is necessary for monitoring or fine registration. The GNSS has been effectively utilized in various applications offering cm or mm accuracy [76–78], while the system can provide great accuracy when it is combined with UAV and t-LiDAR data [46,64].

High-accuracy, dense 3D point clouds can be derived using both UAV–SfM and t-LiDAR methods. The M3C2 (Multiscale Model to Model Cloud Comparison) algorithm [79] is commonly used for point cloud analysis [80]. One key advantage of this algorithm lies in its ability to directly analyze point clouds with no use of mesh or grid, while also estimating a confidence interval based on the characteristics of the point clouds and registration error. The M3C2 process comprises, firstly, an estimation of surface normals and their orientation in 3D space, at a scale consistent with local surface roughness. Additionally, the process calculates the mean surface change along the normal direction, while explicitly calculating the local confidence interval. Advanced research focuses on surface change detection by using point cloud analysis instead of a DEM comparison [81–83].

The DEM of Difference (DoD) [84,85], on the other hand, is a commonly used technique applied in a plethora of scientific research topics [86–89], where multi-temporal DEM can be compared pixel-to-pixel, resulting in surface change detection and volume calculations. Researchers [35] denoted caution in the interpretation of the DoD and recommended using higher-resolution elevation data for accurately quantifying erosion deposition processes. The vegetation canopy is considered a significant limitation for the DoD multitemporal analysis [90], while other researchers [91] denoted that the 3D dynamic processes leading to objects subjected to vertical shifts need to be analyzed in a 3D spatial approach. This article focuses on soil erosion and sedimentation rates on a wildfire-affected mountainous catchment. The methodological approach involved different techniques, each one with its own strong points, weaknesses, and constraints, signifying that a single fit-for-all technique is not often applicable in field studies. In particular, our approach involved three TLS surveys, three UAV campaigns, one GPR, and one GNSS survey, performed during a six-year period. Their utilization, deciphered into soil surface change and sediment yield, provided a highly accurate post-fire measurement of contemporary deposition rates. Overall, this study denotes the capabilities of the UAV–SfM and TLS-derived point clouds in the measurement of high-resolution erosion and sedimentation rates in post-fire conditions. To our knowledge, this subject has yet to be explored and expanded within the scientific community.

2. Study Area and Methodology

2.1. Study Area

The Attica basin is bounded by the mountains of Hymettus, Parnitha, Penteli, and Egaleo. The study area is a 30 ha basin with relatively steep slopes (a 40% average slope dip), located at the SW slopes of the Hymettus mountains, at approximately 500 m elevation, near the Athens Metropolitan area, Greece. The Hymettus mountains suffered a significant wildfire in July 2015. The Difference Normalized Burn Ratio (Figure 1, dNBR) [92–95] index was used to delineate the burnt area by using Landsat 8 pre-fire and post-fire images (Bands 5 and 7). The dNBR vegetation index analysis showed that the area affected by the wildfire spanned 760 ha. This small basin is constrained by a small concrete retention dam that had been constructed approximately 20 years before the recent wildfire in order to reduce the flood events to the city of Athens following an older forest fire. The dam acts as sediment trap, allowing us to measure the sediments that are deposited year by year. This concrete

dam and the surrounding rocks are mostly impermeable. As a result, it always gathers water behind the dam, so it is mostly sedimentation, and this is also verified by the fact that the deposition area is almost flat. The study area used to be covered by shrubs and a small portion of forest trees before the fire of 2015, according to the CORINE 2012 dataset (CORINE Land use code 310, 324, CLC 2012). After the fire of 2015, the whole basin was covered by shrubs and low vegetation. The basin is drained by a relatively sparse hydrographic network with no continuous flow due to the marbles that are the dominant geologic formation and are permeable to water. Therefore, the drainage network is predominantly expressed within the schist formation and is also supported by the relatively steep slopes. Due to the erosive schist formation and the geomorphological characteristics of the basin, the lower part of the watershed is prone to soil erosion. The study area geologically comprises the metamorphic unit that belongs to the alpine basement [96], covered by post-alpine sediments with a relatively steep slope, which, when correlated with lithology, is susceptible to erosion processes. The wider area is part of the Autochthonous Attic–Cycladic Complex unit. The detailed geological structure was derived after extensive field mapping on a 1:10,000 scale, based on the Koropi–Plaka geological map [97] of the Hellenic Survey of Geology and Mineral Exploration (HSGME). The basin geology comprises thick-bedded Jurassic grey marbles overlaid by Jurassic Kaessariani schists with marble intercalations. The schist is extensively deformed, while the marble is found brecciated and karstified. Well-cemented conglomerates with claystone intercalations (originating from the marbles) and alluvial fans are traced along the stream network. Localized talus cones can also be found within the schist, where the surface slope and the schist inclination are dipping towards the same direction. Additionally, Terra Rossa (Calcic Haploxeralfs or Calcic Luvisols) is a red-type formation constituting a typical soil in the Mediterranean region, generated on carbonate rocks. It is noted that the schist is covered by a weathered mantle of significant thickness. Where there is no sufficient soil depth, the soils can be categorized as Leptosols (in some regions nudilithic Leptosol can also be found), consisting of shallow calcareous soils, originating from marbles, usually found on slopes. Soil coming from the local schist is more yellow–grey Cambisol with low organic content. Finally, anthropogenic deposits were delineated and excluded from the soil erosion assessment (Figure 1).

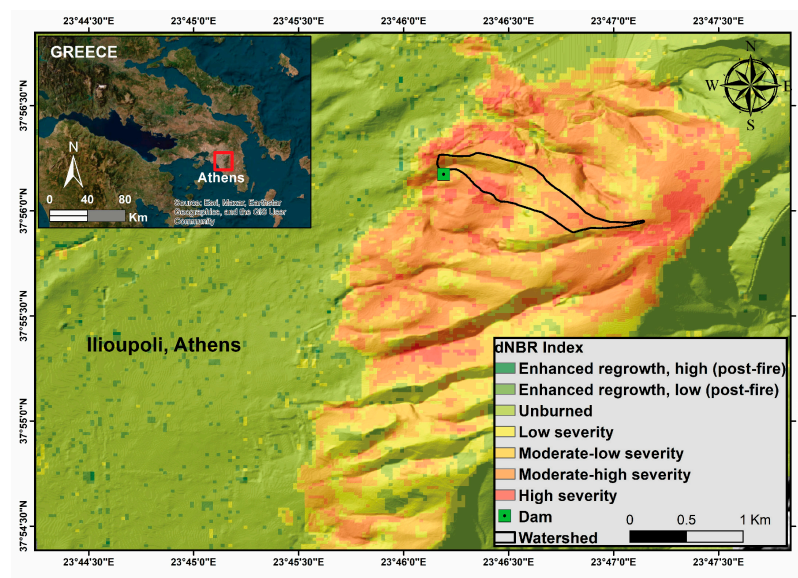


Figure 1. Cont.

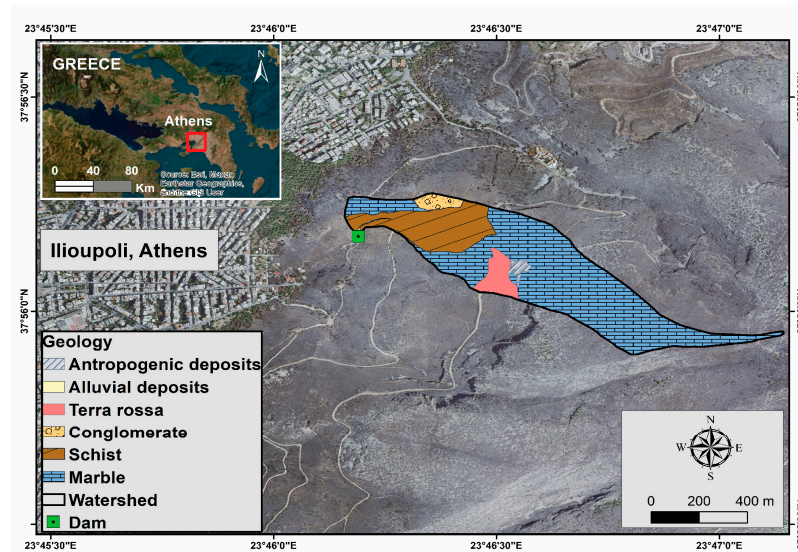


Figure 1. dNBR index (processed with Google Earth Engine) following the wildfire event of 2015 and geological map of the study area (scale 1:10,000 based on HSGME 1:50,000 Koropi–Plaka geological map [97]).

2.2. Data and Measurements

2.2.1. Data Collection Timeframe

Soil erosion and sedimentation monitoring in the Ilioupoli test site was performed from 2015 to 2021 and was focused near the dam area. The methodological framework included UAV, t-LiDAR, and GNSS point cloud analysis (2015–2021) combined with the GPR results (2016). The proposed methodology includes a combination of different emerging tools when limitations exist (e.g., vegetation growth following a wildfire event). The final products (point clouds) were then correlated to each other leading to sedimentation measurements. The simplified study workflow is summarized below in Figure 2.

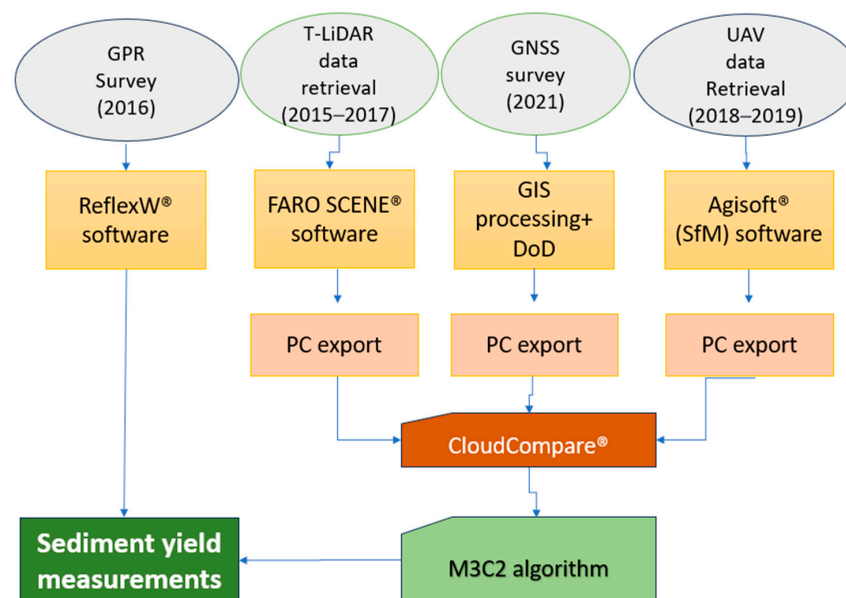


Figure 2. The simplified study workflow.

Since 2015, different sediment yield monitoring systems have been deployed due to technological advances and limitations (Table 1, Figure 3). The study framework comprises the four main methods of remote sensing and geophysical analysis. First, the t-LiDAR

method focusing on 3D surface reconstruction was performed in different timescales, in 2015–2016–2017. Second, the geophysical GPR method focusing on high-accuracy subsurface structure definition took place in 2016. The third technique concerns the UAV–SfM, which denotes the geomorphological change detection in the temporal period based on a high-accuracy photogrammetric technique, and, finally, the geodetic topographic method GNSS (in 2021) focusing on precise ground point measurements. Three t-LiDAR field campaigns were carried out in 2015, 2016, and 2017. The first one was held in October 2015 (Figure 4) and the second in April 2016. Subsequently, the last t-LiDAR field campaign was conducted in January 2017, for the generation of a new point cloud following the excavation and removal of sediments below the dam. Local authorities removed the existing sediments and widened the upland dam area used to prevent potential flood events into the city. Therefore, the previously collected data in 2015–2016 were only used for the 2015 and 2016 sediment estimations. During the field work in April 2016, the GPR method was also applied (Figure 5). Two UAV–SfM field campaigns were held in August 2018 (31 August 2018) and in March 2019 (18 March 2019), followed by a GNSS survey (also in 2019) for the GCP georeference, while the third campaign in 2020 did not prove fruitful for achieving the required cm accuracy, due to excessive vegetation growth and, as such, it was disregarded. The type and technical specifications of all sensors are summarized in Table 2. The TLS and photogrammetry methods used have also been thoroughly described in [46].

Table 1. The data collection timeframe.

Date	Acquisition Type
July 2015	Wildfire event
October 2015	LiDAR
April 2016	LiDAR
April 2016	GPR
January 2017	LiDAR
August 2018	UAV–SfM
March 2019	UAV–SfM
August 2020	UAV–SfM
April 2021	GNSS RTK System



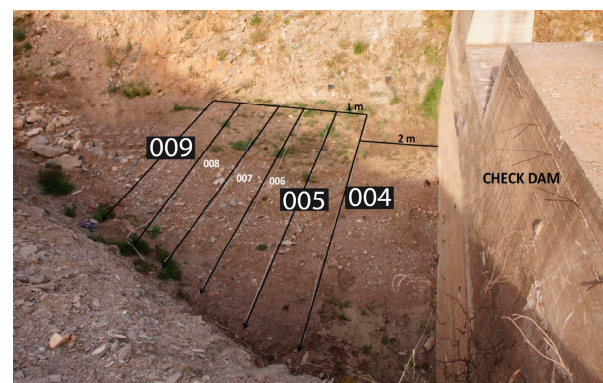
Figure 3. View of the retention dam following the wildfire event in 2015.



Figure 4. The retention dam following the wildfire event in 2015 during the first t-LiDAR survey in October 2015.



(a)



(b)

Figure 5. The GSSI and SIR model 3000 system (a), the GPR-derived six survey profiles in April 2016 (b).

Table 2. The technical specification of all sensors used in this study.

	t-LiDAR Sensor	UAV Sensor	GPR	GNSS RTK Receiver
Sensor	FARO FOCUS 3D	DJI Phantom 4	GSSI and SIR 3000	Spectra SP60
Basic specifications	0.6–330 m distance range	1/23 12.4 MP, FOV 94° lens @20 mm camera sensor	400 MHz antenna	RTK position
	Ranging error: ± 2 mm	4000 \times 3000 image analysis	0–4 m depth range	0.017 m vertical accuracy 0.008 m horizontal accuracy

2.2.2. The t-LiDAR Surveys

This technique is focused on the point cloud creation, derived by the LiDAR method to describe surface geometry. In our case, the small-scale soil topography has changed since the wildfire event, due to the surface water overflow and the topsoil (surface mantle) properties. For this purpose, the FARO FOCUS 3D LiDAR sensor was used (Figure 4).

Four scans were aligned for the final 2015 scan and two scans were aligned for the year 2016. Both clouds were subsampled, resulting in over 4,000,000 points for each final point cloud. The 2015 point cloud has a surface density of 790 points/m², while the 2016 point cloud has about 1000 points/m². The 2017 t-LiDAR scan comprised two separate scans, resulting in a point cloud of over 8,000,000 points with a surface density of 1000 points/m².

Each scan of the total watershed was initially processed through the FARO SCENE software, provided with the FARO FOCUS 3D sensor. The software performs a basic automatic registration based on the common features between the scans. The object detection and the registration of the scans was supervised and assessed by the TLS operator. The 2015 and 2016 total scans were used for qualitative purposes and no ground point classification was performed. Points attributed to vegetation cover were manually removed, point by point.

The 2015, 2016, and 2017 scans used for the sediment measurements within the dam area were derived from one scan location within the dam area (see also Section 3: Results, red arrows in Figures 10 and 16). The final point cloud analysis was performed in the CloudCompare environment. The georeference of all scans within the dam area was based on GNSS measurements and the GCP location surveyed by the Spectra Geospatial SP60 GNSS RTK sensor (Figure 6a) in the Greek Grid (EPSG: 2100) coordinate system.

2.2.3. GPR Data Collection

For the sediment deposition's validation analysis, GPR data were collected by the Institute of Neotectonics and Natural Hazards, RWTH Aachen in 2016. The goal was to define the depth of the contact between the bedrock and the sediments based on their different density properties. Through the bedrock depth estimation, the sediment infill can be calculated.

The GSSI GPR system and the Geophysical Survey System (SIR) model 3000 was used [98]. The monostatic 400 MHz antenna that was selected (Figure 5a) can achieve about 4 m penetration depth [99]. When the single antenna mode is preferred, the transmission mode changes simultaneously to the reception mode [100]. The survey wheel is a receiver and a pulse generating sensor that also sends the signal for the antenna mode transition. Data processing was performed using the ReflexW[®] software (v. 7.5) from Sandmeier Scientific Software, Karlsruhe, Germany. The processing sequence involved several steps, including removing header gain, adjusting start time, addressing energy decay, applying a 1D bandpass frequency filter, and removing background noise. The upland dam basin was excavated in August 2015 following the wildfire event of July. The survey took place in April 2016. During the field survey, six survey dam-parallel (W-E) profiles along the dry-to-moist sandy basin dam were retrieved. The first profile was defined at a 2 m distance from the dam, while the successive profiles had an interspacing distance of 1 m from each other. The boulders that were visible in the middle of the dam during the first fieldwork in 2015 have now been buried by the sediments visible in April 2016 (Figure 5b), highlighting the sedimentation processes [98].

2.2.4. UAV Image Acquisition and Processing

The operator selected to set the flight plan during the study area visit and used the nadir camera orientation mode due to the dam basin's flat surface in a constant flight above ground level (AGL). The AGL was maintained at the same level in every flight plan, so as to achieve a high Ground Sampling Distance (GSD). Finally, the flight height was set to 15 m AGL (5.76/pixel GSD) and remained constant in every later accomplished flight plan.

The first flight survey was conducted on 28 September 2018 and an additional flight took place six months later in March 2019. The 2018 flight survey resulted in 93 photos; 127 photos were captured on 18 March 2019. During the UAV surveys, 10 GCPs were used as stable Ground Control Points. Since only nadir photos were captured, we selected to apply more GCPs to decrease the dome effect and achieve a higher accuracy [101,102]. The GCPs were placed in stable ground points such as the dam's crest and bare exposed bedrock. The

GCPs were spread as evenly as possible across the upland study area (Figure 6a). Following the definition of the GCPs, the SP60 Real-time Kinematic Positioning Global Navigation Satellite System (RTK GNSS) was used to retrieve their coordinates for georeferencing and accuracy assessment reasons. The GNSS sensor accuracy reaches <1 cm in the horizontal plane and 1.7 cm in the vertical axis. Flight planning and operation were performed on DJI GS PRO. This data collection technique is considered adequate for this type of surface reconstruction following a detailed error assessment procedure. The acquired images were photogrammetrically processed using Agisoft PhotoScan Metashape Professional from Agisoft LLC, Petersburg, Russia (v. 1.5.5). The defined flight height and the GSD resulted in high-accuracy-derived products (dense cloud, DEM, and orthomosaic, Table 3, Figure 6). This test site is characterized by great 3D modeling due to the low altitude flight of the UAV and the restricted upland dam area.



Figure 6. Agisoft orthomosaic derived by the DJI Phantom 4 UAV–SfM surveys on 31 August 2018 (a) and 18 March 2019 (b). The location of the GCPs is depicted in yellow in the 2018 orthomosaic (a).

Table 3. Agisoft product resolutions (mm/pixel).

Product	Resolution mm/pix	
	31 August 2018	18 March 2019
Tiled model	4	1
DEM	20	12
Orthomosaic	5	5.8

2.2.5. The GNSS Survey

The ground truth authentication and observation methods were selected using the GNSS technique. The GNSS survey was performed on 23 April 2021 and was analyzed in a GIS environment and CloudCompare software. The points were surveyed by the GNSS receiver, projected in the EGSA '87 Greek Grid, EPSG 2100 coordinate system. It was considered the most adequate solution for the high-accuracy microtopography reconstruction due to the 2021 extended vegetation cover obscureness. This was facilitated by the well-constrained, relatively short area of about 280 m², where sediments are deposited behind the dam. Our intensive field study led to 5600 points being measured within the dam upland area in an interspace distance range of 0.10–0.40 m, depending on vegetation obstacles. The data collection was performed with the Spectra SP60 RTK GNSS deployed in Real-Time Kinematic (RTK) mode. The RTK method was selected, where the continuous automated step of measuring points was defined in 5 s intervals, via the Survey Mobile software. The mean distance between the measurements was about 20 cm (resulting in 5600 points), so the vertical position of the pole was achieved through the mounted level arm. The ground truth was achieved through the stable reference network JGC-net. The spatial resolution reached 0.008 m horizontally and 0.017 m vertically. The DEM was

derived after the manual removal of outlier points in the ArcGIS environment (v.10.8) and the point cloud was processed in CloudCompare. By using the real point data obtained with the manual measurements and by applying the kriging interpolation method, a DEM was derived with a spatial resolution of 0.01 m (Figure 7). Other studies also use Geodetic data for measurements or references [103–105].

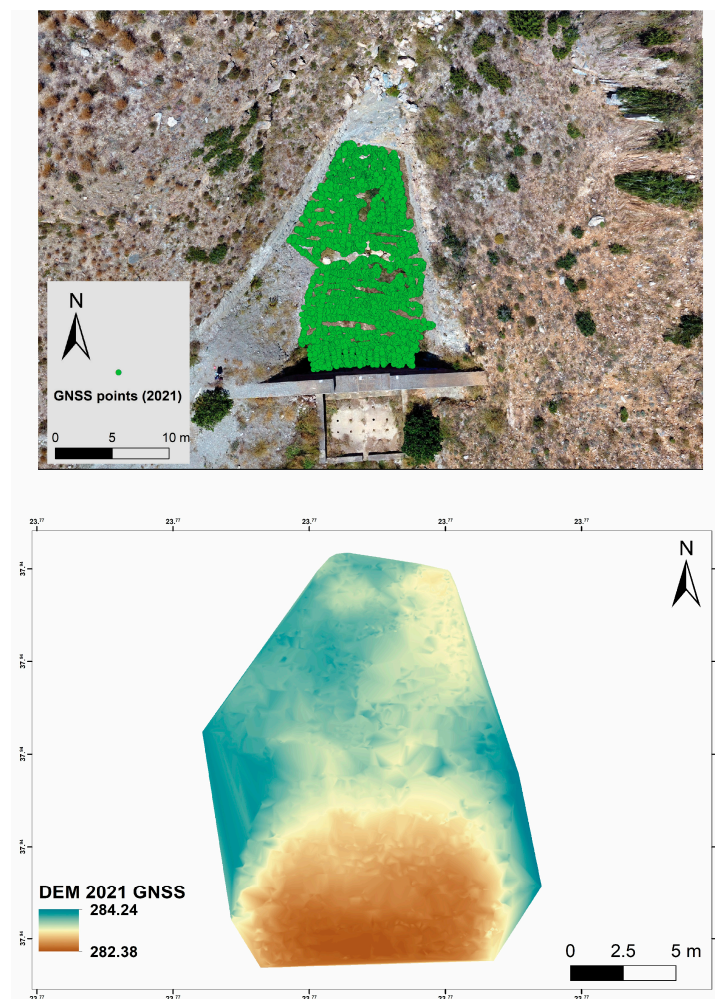


Figure 7. A total of 5600 GNSS points were retrieved during field measurements in 2021, resulting in a GNSS-derived DEM of 1 cm pixel size.

2.2.6. Point Cloud Processing

The distance calculation method M3C2 was utilized [79] through the CloudCompare software. This algorithm integrates the local distance between two point clouds in conjunction with the detection of normal surfaces, which effectively tracks 3D variations in surface orientation. Employing the M3C2 algorithm and computing the vertical normals, we conducted comparisons between point clouds of all techniques (Figure 2). After the experimental use of different values and the “guess params” option (provided by the software), we concluded a 0.20 m normal scale diameter and a 0.10 m projection scale diameter.

DoD on the other hand, is also considered a widely used method resulting in accurate estimations. The 2021 GNSS-derived points were compared to the 2017 t-LiDAR-derived DEMs for the 2021–2017 sediment yield DoD estimation. By applying the kriging interpolation method, all DEMs were derived with a spatial resolution of 0.01 m in order for the results to be comparable. Recent research has also explored how the impact of DEM resolution, or point spacing (in grid format), influences the estimation of erosion and deposition volumes by using high-accuracy t-LiDAR data. Lu et al. [106] examined the impact of grid

size on hillslope erosion and deposition based on t-LiDAR-derived DEM, highlighting that the changes in erosion seem to be less sensitive compared to the changes in deposition, while other similar results in a gully erosion study denote that very-high-resolution DEMs enhance local errors, overpredicting the gully erosion extent [107]. As [108] denoted, a 3D point cloud analysis is considered more accurate in surface change detection due to the individual point processing, compared to the 2.5D grid elevation data (DEM) analysis.

As a result, our study focuses on point cloud analysis and high-accuracy point measurements, while the DoD is used only for comparison purposes (2021 and 2017 data) and the cross-section analysis of 2017, 2018, 2019, and 2021 data (Figures 11, 12, 18, and 19).

3. Results

3.1. Point Cloud Analysis

Two point cloud dataset analyses were deployed. The first survey was accomplished within the period 2015–2016 and the second covered the period 2017–2021.

3.1.1. The 2015–2016 t-LiDAR analysis

The 2015 and 2016 analysis included the first qualitative comparison of the full t-LiDAR scans (Figure 8a,b). Due to the lack of GCPs covering the total basin, the full 3D point clouds were only used for the qualitative surface change detection. The results showed a good correlation to the field observations. The eastern slopes over the road (western aspect), where schist forms a significantly weathered mantle (Figure 9, inside the red circle), appear to be the most erosion-prone formation, in accordance with our expectations.

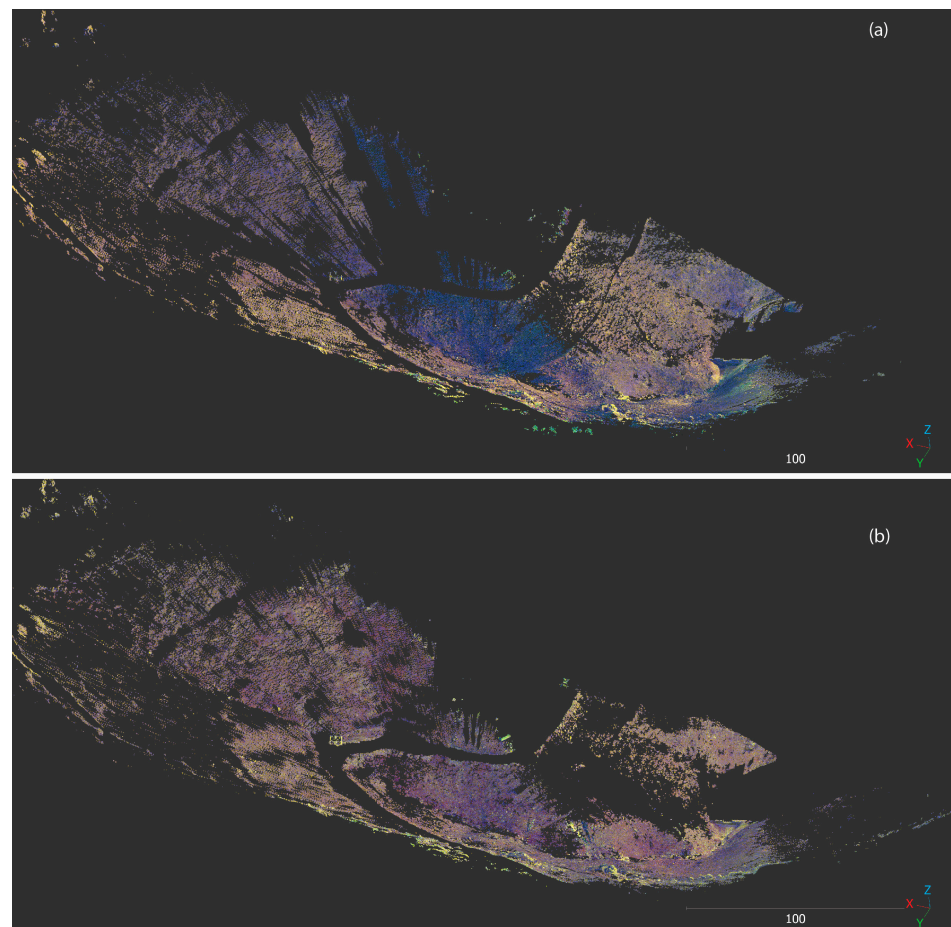


Figure 8. The FARO LiDAR complete scan deployed in 2015 (a) and in 2016 (b).

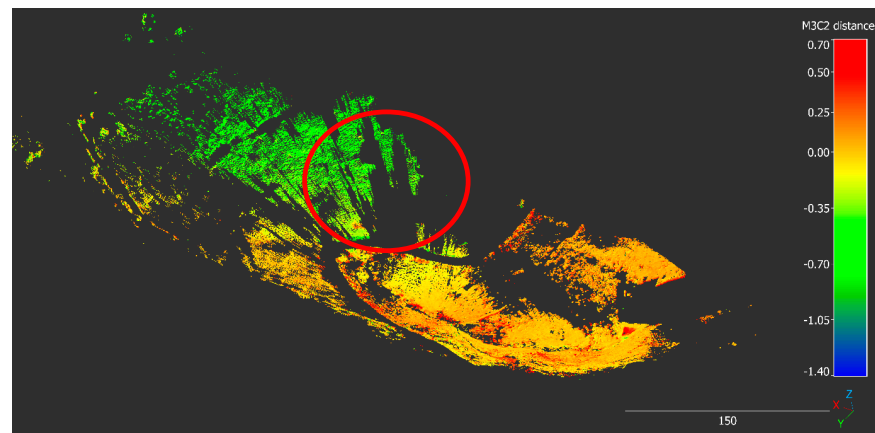


Figure 9. The M3C2 vertical difference (m) for the years 2015 and 2016 for qualitative analysis, depicting erosion-prone sites in green (in the red circle), and deposition sites in orange/red.

The M3C2 algorithm of vertical difference detection (processed in CloudCompare) between 10/2015 and 4/2016 point clouds (Figure 10a,b) revealed a mean sediment surface deposition of 0.48 m (Figure 11), which corresponds to 23 m³ of the total sediment deposition within an area of 48 m². The above-mentioned conclusion is in accordance with the rasterized volume calculation (without interpolating empty cells) of 20 m³ (Figure 12). The sediment deposition is depicted in the profile view in Figures 13–15.

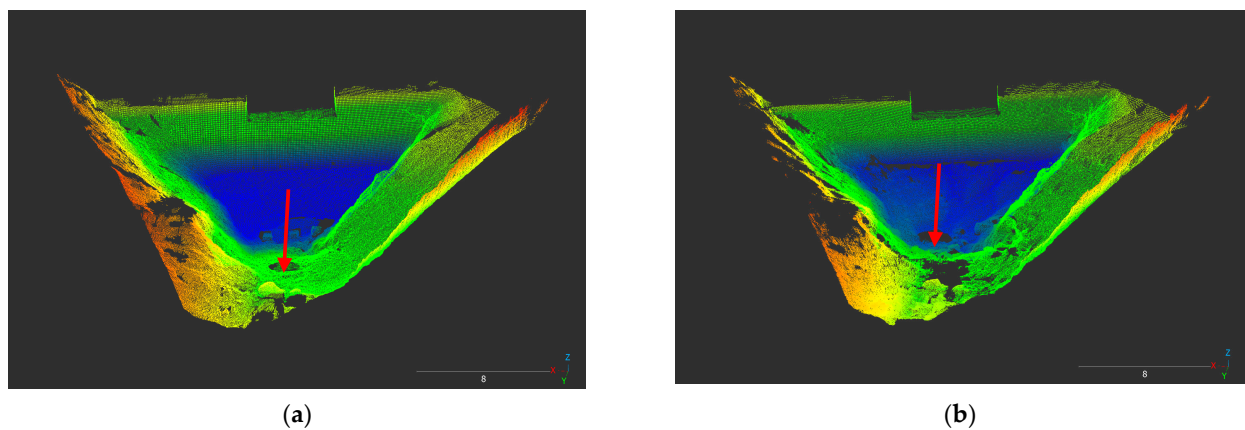


Figure 10. The simplified 2015 (a) and 2016 (b) LiDAR scans focusing on the dam upland area. The red arrow indicates the FARO scanner location.

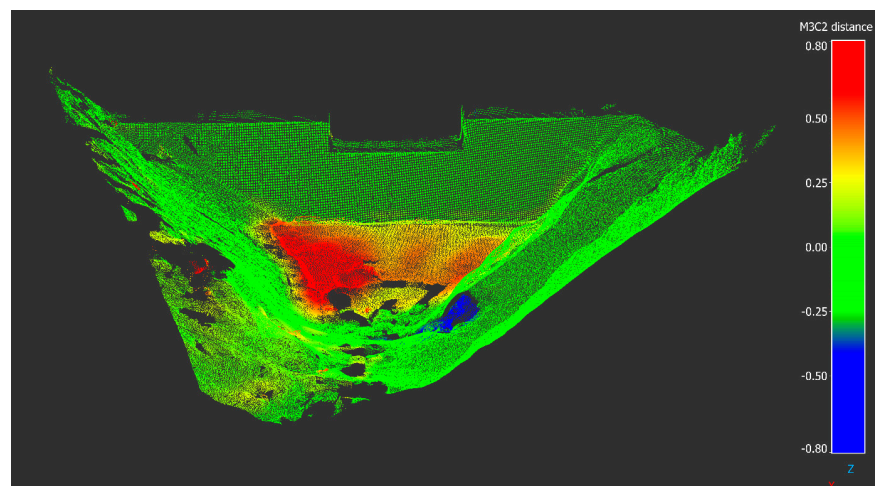


Figure 11. M3C2 vertical difference (in m) for the years 2015 and 2016.

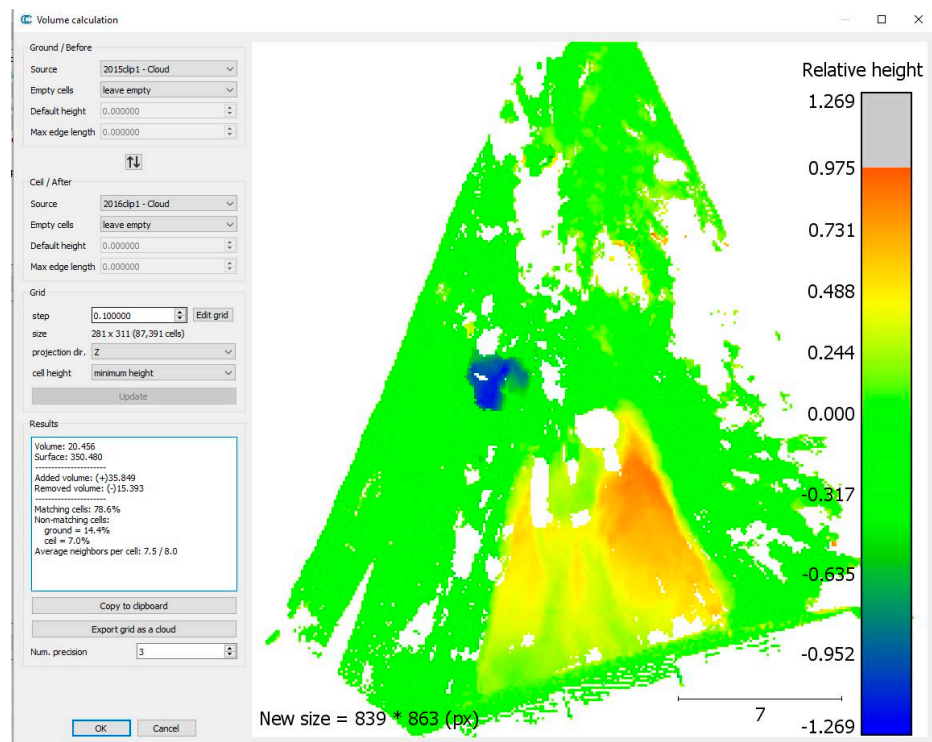


Figure 12. Calculated deposition volume of about 20 m³, through the CloudCompare software implication.

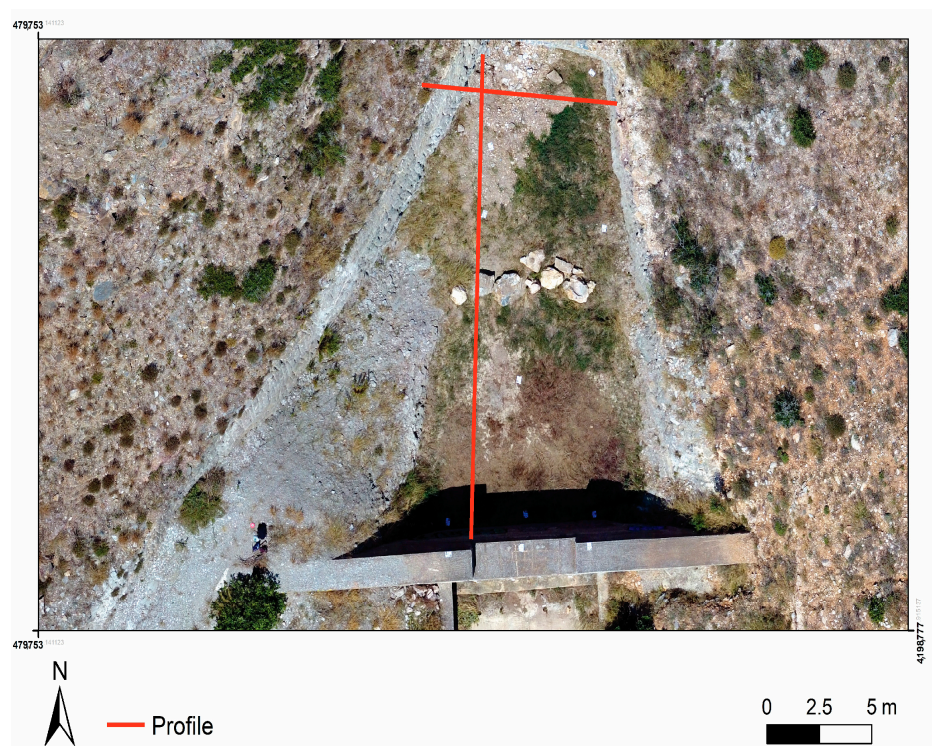


Figure 13. N-S and E-W profiles (red lines) depicted on the 2018 UAV-SfM-derived orthomosaic.

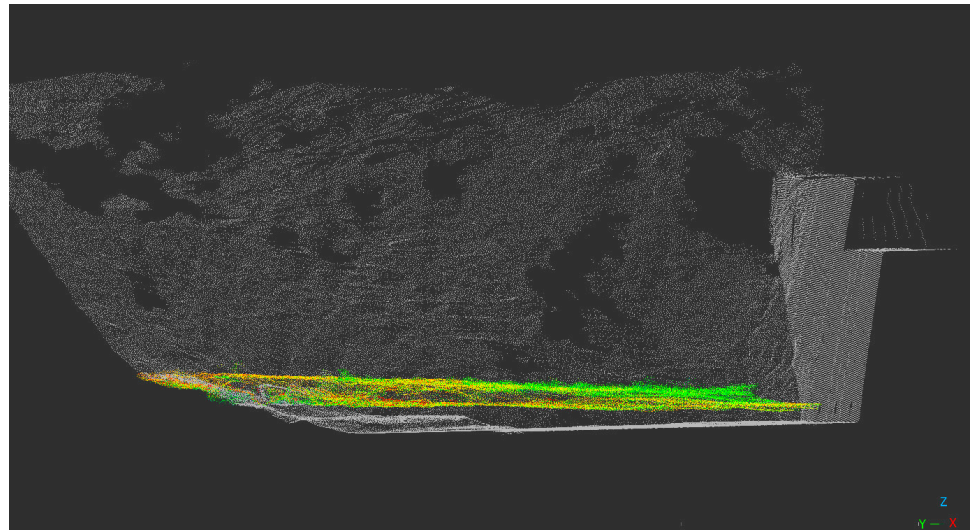


Figure 14. N–S profile of the 2016 deposition in the upland dam basin. The grey point cloud represents the 2015 reference scan.

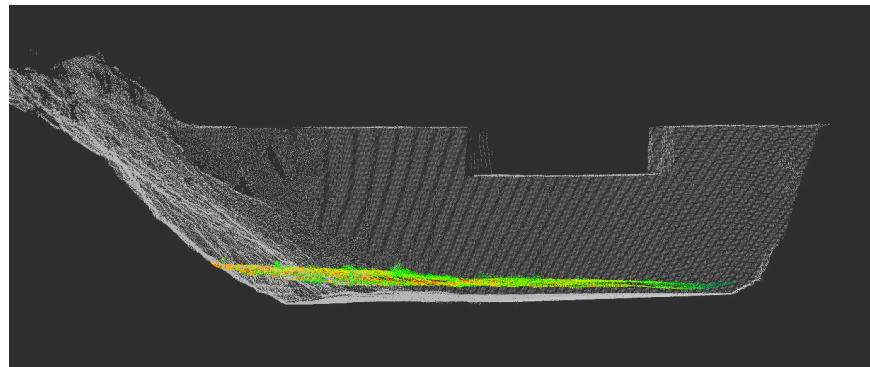


Figure 15. E–W profile of the 2016 deposition in the upland dam basin. The grey point cloud represents the 2015 reference scan.

3.1.2. The 2017–2021 Point Clouds Analyses

The 2017–2021 dataset analysis includes a 2017 LiDAR-derived point cloud, two UAV–SfM-derived point clouds of 2018 and 2019, and the 2021 GNSS points (Figures 16 and 17).

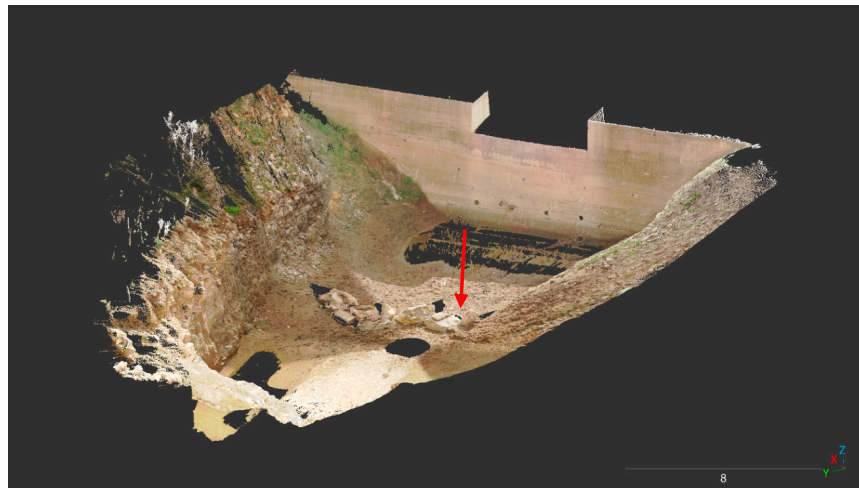


Figure 16. The FARO LiDAR scan deployed in January 2017. The red arrow indicates the FARO scanner location.

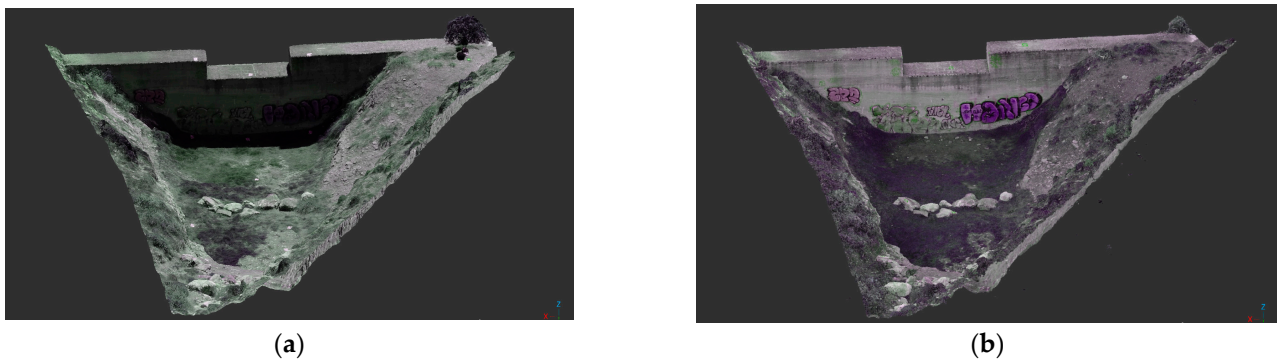


Figure 17. The UAV-SfM-derived point cloud in August 2018 (a) and in March 2019 (b).

The DoD method revealed a maximum surface deposition of 0.79 m (Figure 18a), corresponding to the areas of soil mass movement at the eastern boundary of the dam. The predominant soil loss pattern encompasses regions where large rocks are present, acting as barriers to water flow in a north-to-south direction. As a result, the water velocity increases on both sides of these rocks. The mean 2017–2021 vertical difference of the points (Figure 18b) reaches 0.06 m according to the Gauss distribution, covering an area of 150 m² or a mean volume of 9 m³. The net deposition also follows the Gauss distribution, characterized by a mean value of +0.1 m or 15 m³.

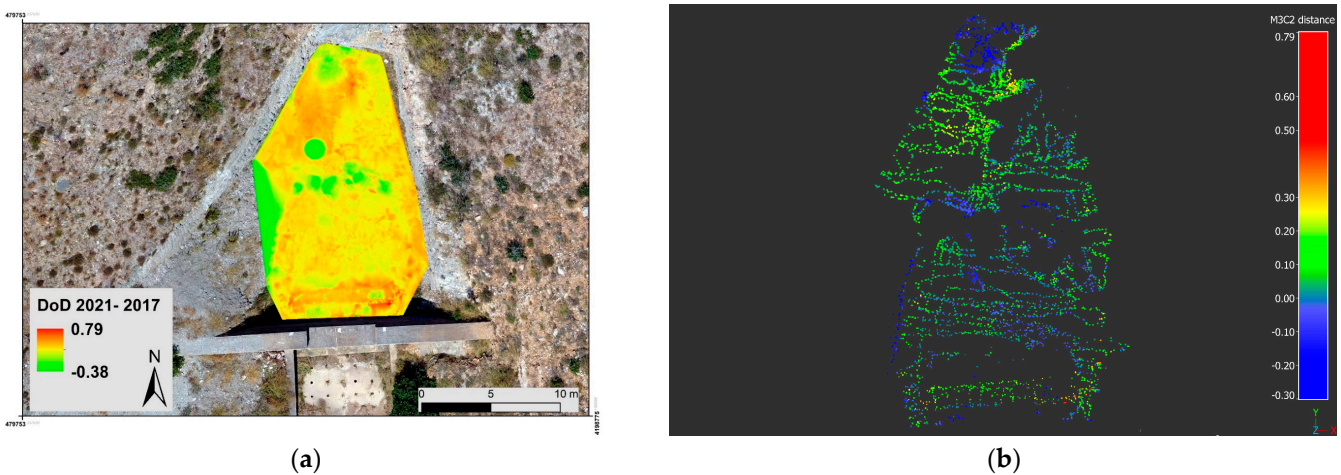
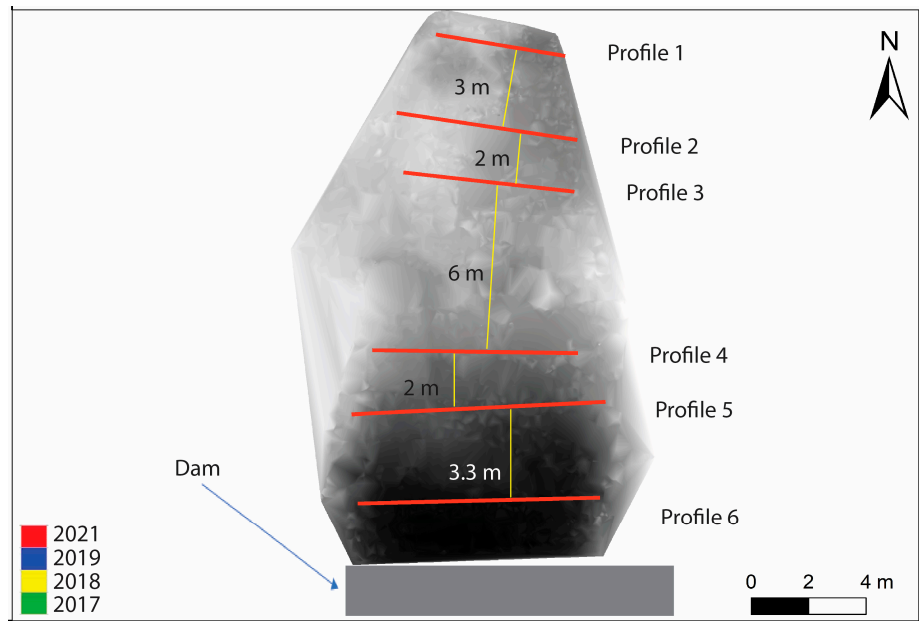


Figure 18. The DoD (a) and the M3C2 vertical difference (in m) (b) for the 2021 and 2017 comparison.

Six profiles were constructed based on the 2017, 2018, 2019, and 2021 derived DEMs to compare the annual microtopography change. Profile 1 was constructed 18 m north of the dam, being the most distant from the dam, while the next five profiles were almost parallel to Profile 1 (all in a W–E trending direction) within a distance of 2–6 m from each other (Figure 19) that was constrained by the vegetation coverage. All six profiles are placed in the W–E direction and are represented by red lines traced on the 2021 DEM. Profile numbering (1–6) starts from one that is the most distal profile from the dam, and then profile numbers increase progressively as approaching the dam. The figure below includes 2021, 2019, 2018, and 2017 profiles delineated for the same red cross-section. The 2021 DEM is represented by the red line and the 2017 LiDAR DEM is represented by the green line in the cross-section diagram (Figure 19). The 2018 and 2019 UAV-SfM-derived DEM are represented by yellow and blue cross lines, respectively.



Profile 1



Profile 2

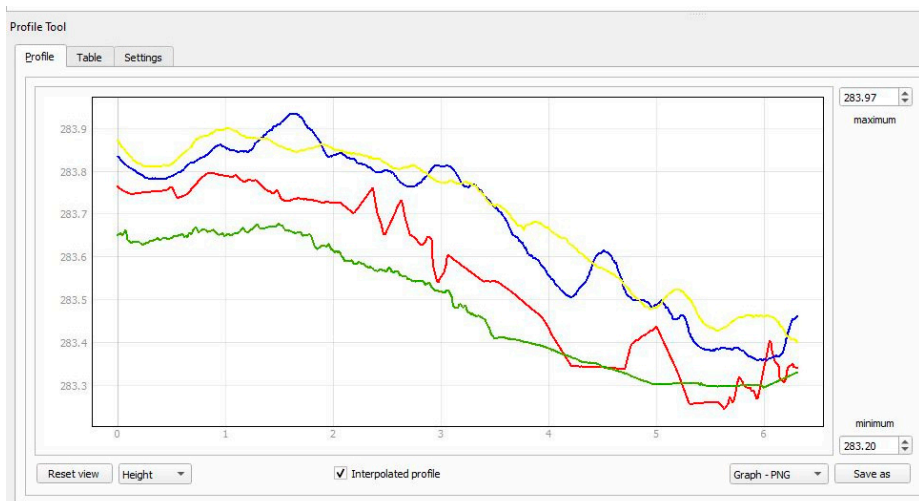
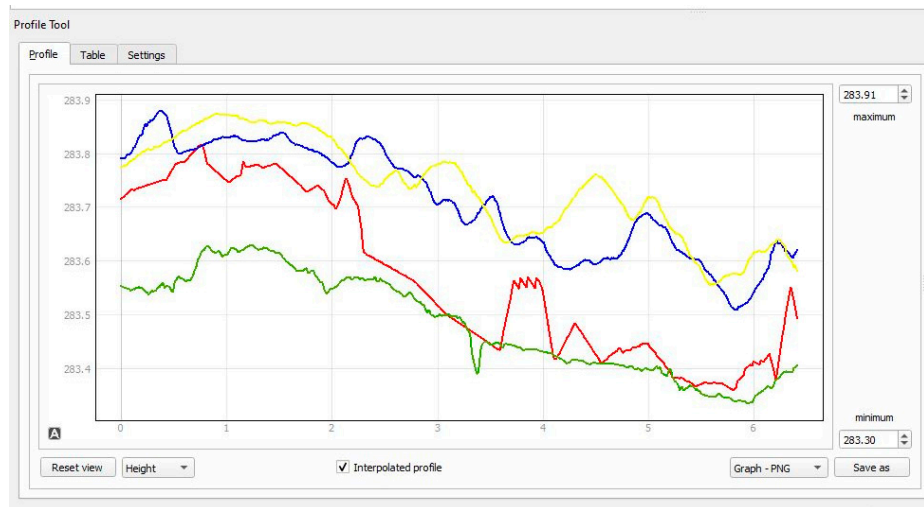
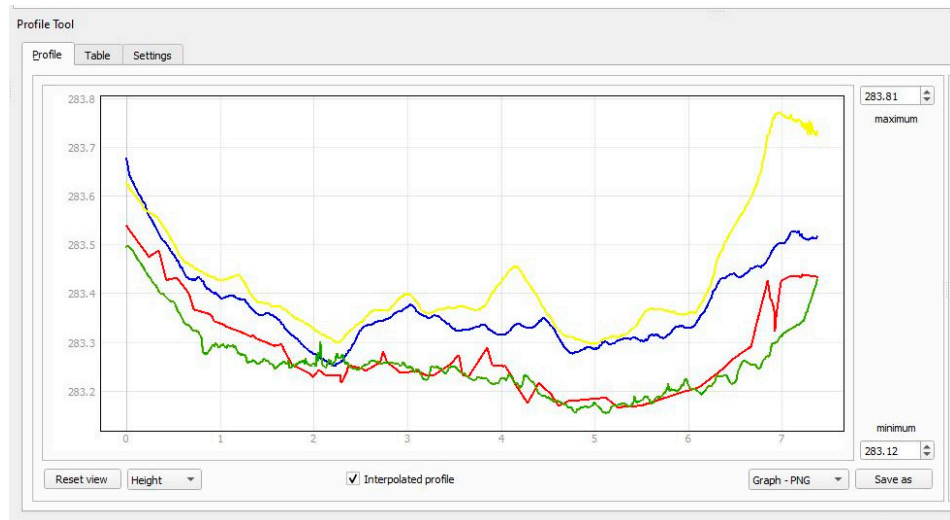


Figure 19. Cont.

Profile 3



Profile 4



Profile 5

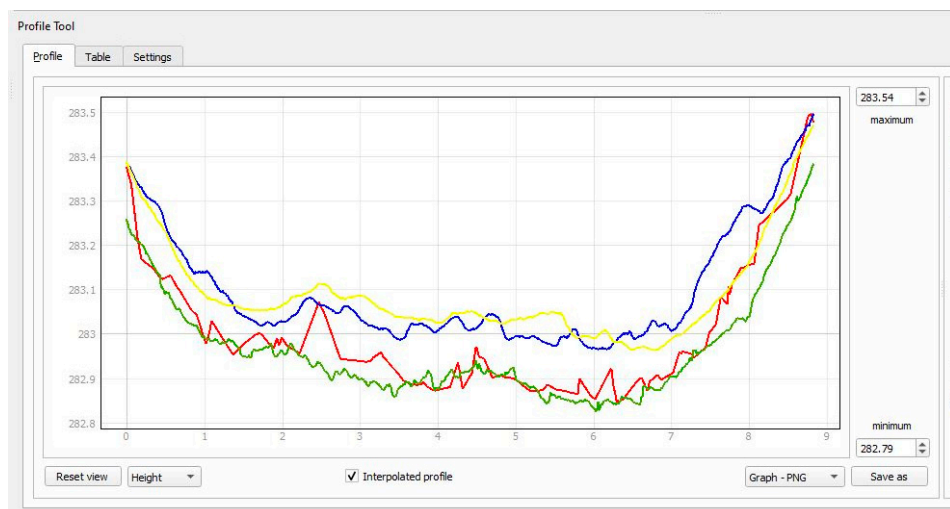


Figure 19. Cont.

Profile 6

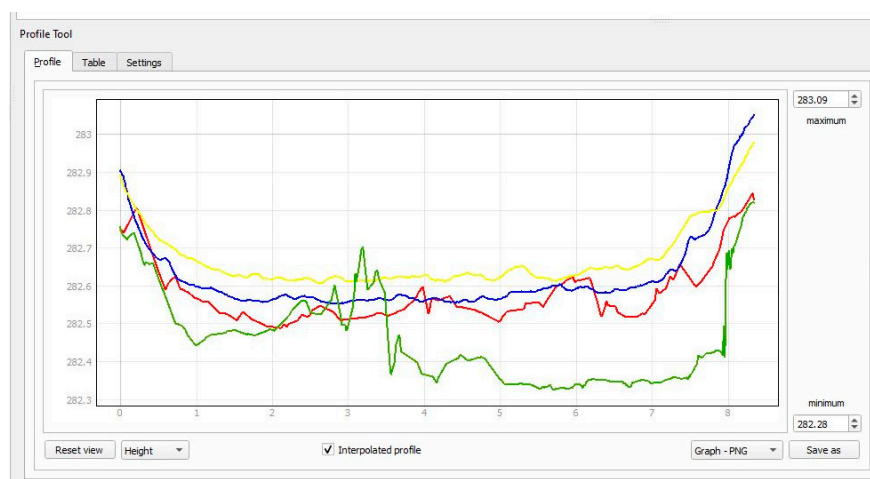


Figure 19. View of the 2021 DEM, showing the traces of the cross-sections and detailed cross-sections 1–6 within the upland dam area, representing the surface change for the years 2017, 2018, 2019, and 2021.

The green line is basically the reference surface of 2017. At Profile 1, the most distant from the dam, we can note that the red line of the 2021 surface is mostly placed below the 2017 reference point, highlighting the local erosion processes in this area. This is modified in the following profiles as approaching the dam, where the red line is mostly above the green line. In particular, Profile 6 shows that approximately 20 cm of sediments were deposited in the central and eastern part of the dam from 2017 up to 2021. The latter signifies that the sediments were transported from the area of Profile 1 and were redistributed closer to the dam in the upcoming years. Overall, Figure 19 depicts the spatiotemporal evolution of the sediment supply, transportation, and redistribution, also offering important insights into sedimentation processes. Profile 6 denoted the position of the main sediment deposition in front of the dam.

3.1.3. Error Assessment

The registration error refers to the point cloud registration to a reference cloud. The GPS points were often used as the reference points to where each LiDAR-derived point was assigned to. In the case of the 2016 point cloud, 2015 was the reference to achieve the best cloud alignment and accuracy (Table 4). The XYZ error analysis procedure is thoroughly described in Alexiou et al. [46].

Table 4. Summarized error analysis for each point cloud dataset.

Point Cloud	Reference Points	Registration Error (cm)	XYZ Error (cm)	Total Error (cm)
2015	GNSS 2019	5	5	5
2016	2015 LiDAR	3	5	5
2017	GNSS 2021	1	2	2
2018	GNSS 2019	3	2	3
2019	GNSS 2019	3	1	3

3.2. The GPR Results

The radar profiles in Figure 5b (such as No. 004 in Figure 20) are composed of three or even four significantly distinct layers [98]. We focus on the upper 2 m because the expected structures are expected in the upper subsurface (<2 m). The lower 2 m are free of reflections due to the possible air wave reflections from the dam. Facie 2 is a horizontal, parallel-to-surface reflection at a 1 m depth. There is also a distinct reflection near the surface (Facie 3) which seems to be parallel to Facie 2. Both are considered continuous

structures (Figure 20). The deepest point has been found at a 7 m distance at a 1.4 m depth. Facie 3 occurs at a depth from 0 m up to 0.6 m. There is also a Facie 4, where no reflections occur at a depth of 1.8 m (at a 3–4 m distance, [98]).

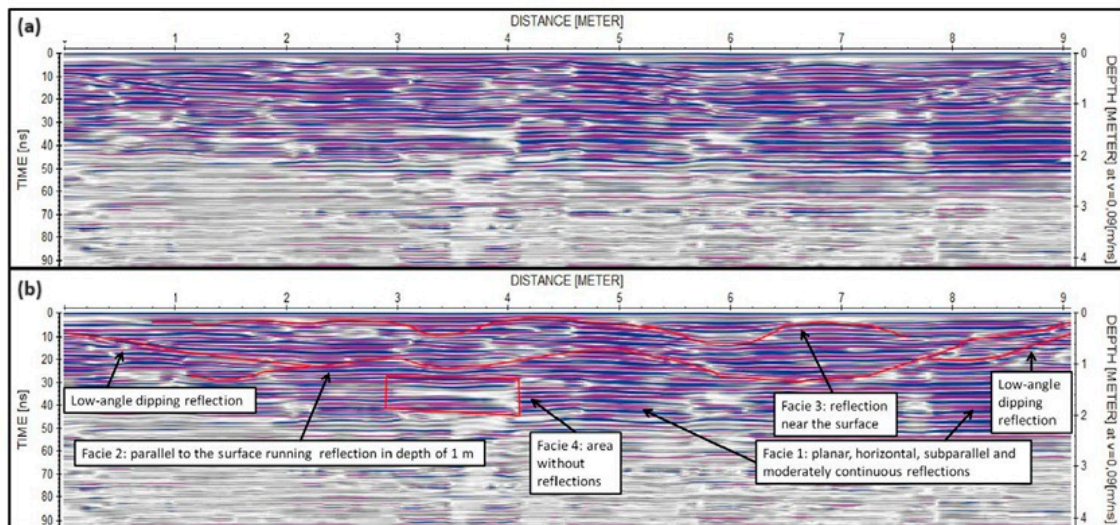


Figure 20. Analysis of profile 004. (a) Processed radar file and (b) processed file with highlighted radar facies and a short description of them [98].

Facie 1 in radar profile 004 is horizontal, continuous, and parallel, attributed to the plane basin deposition (Figure 20). Facie 2 is a continuous structure denoted along the whole radar profile. Its depth ranges from 0.7 m up to 1.3 m. The dipping structures at the boundaries of the profile could be attributed to the basin sidewalls. Facie 3 could be highlighting an erosion event and Facie 4 occurs in 1.8 m depth, that could be assigned to bedrock.

The basin dam was excavated in 2015, following the wildfire event of July 2015 (possibly in August 2015). As a result, Facie 2 represents the bedrock, and all the material above this reflection is considered to be the remaining sediment yield that was deposited until April 2016 when GPR profiles were deployed. The corresponding dam basin area is 56 m^2 , which, when multiplied by 1 m mean depth (Facie 2), results in a total volume of 56 m^3 (range $39.2\text{--}72.8 \text{ m}^3$ for a 0.7–1.3 m depth range). For a defined electromagnetic wave velocity, $v = 0.09 \text{ m ns}^{-1}$, the material could be a mixture of unsaturated sand and gravel, unsaturated silt, and unsaturated clay, which is also validated from the soil sampling analysis (Table 5). It should be noted from weather reports that a 36 mm rainfall event occurred in the middle of March 2016, before the GPR method was applied [98].

Table 5. Laboratory results of the Ilioupoli test site’s soil samples (dam area).

Ilioupoli Test Site	DATE	SAND (%)	SILT (%)	CLAY (%)	Soil Texture Class	OM (%)	pH	Electrical Conductivity ($\mu\text{S/cm}$)
Sample Code								
13_dam (4)	2022	46.02	32.42	21.56	L	5.60	8.10	242
14_dam (3)	2022	49.66	19.94	30.40	SCL	4.80	8.10	256
15_dam (2)	2022	70.02	13.70	16.28	SL	1.10	8.20	126
16_dam (1)	2022	46.40	31.14	22.46	L	6.70	8.00	279

To conclude, according to the GPR method, Facie 3 could be assigned to the first sediment deposition event following the wildfire, resulting in a deposition of almost 20 m^3 (17 m^3), while the total sediment measured by the GPR since the dredged basin period till

the day of the measurement reached almost 60 m³ (56 m³). The t-LiDAR method revealed a 20 ± 3 m³ deposition for the period 10/2015 up to 4/2016, showing a good correlation to the GPR results. The t-LiDAR/GNSS comparison analysis for the 2017 (t-LiDAR)—2021 (GNSS) timeframe resulted in a mean deposition of 0.06 m or 9 m³ in total (for the measured surface of 150 m²), leading to 2.25 m³/year (four years in total). This annual value of almost 2 m³ is also validated by the UAV method for the year 2018–2019 (Table 6).

Table 6. Total analysis of sediment deposition.

Date Range		Method	Sediment (m ³)
From	To		
Dredged (~8/2015)	4/2016	GPR	56
10/2015	4/2016	t-LiDAR	20
2017	2021	t-LiDAR-GNSS	9
2018	2019	UAV-SfM	2
Total 2015–2021			65

4. Discussion

Water-induced soil erosion is a prevalent environmental occurrence that has a considerable influence on the viability of agricultural lands, the vegetation regeneration potential of burned areas in natural ecosystems, and the overall stability of landscapes. This article emphasizes the importance of emerging technology in soil erosion and sedimentation monitoring in post-fire settings. By comprehending analysis of the soil-erosion-prone areas, we can formulate effective strategies to mitigate the erosion and to foster soil conservation.

A recently burnt Mediterranean catchment, the Ilioupoli test site, was selected following the wildfire event of 2015. The test site is characterized by a rapid vegetation recovery over the following years that added several constraints to our sediments quantification assessment and, as a result, different techniques have been incorporated.

Advanced methods for soil properties, soil surface conditions, and soil erosion assessment constantly improve both spatial and temporal soil erosion analysis [109,110]. In our study site, several different field work techniques were applied, the UAV photogrammetry and t-LiDAR methods combined with GPR and GNSS data. These techniques result in point clouds that are considered the baseline for the production of 3D models to reconstruct surfaces under a defined coordinate system (local or global), leading to real-time field monitoring. The combination of these techniques has provided the best results, since several constraints appeared along the way. The use of different methodologies, where applicable, is often the only solution to monitor the multi-temporal geomorphological changes, resulting in an accuracy of a few centimeters. Optimal study sites are areas of limited or no vegetation. These sites relate to post-fire settings, settings controlled by overgrazing [111–118], or areas of high sedimentation, where eroded, transported sediments constantly cover the recently formed vegetation (as at the Platana test site [47]). To our knowledge, no detailed soil erosion investigation has yet been conducted regarding the combination of UAV- and t-LiDAR-derived point cloud algorithms in fire-affected areas.

Both techniques have advantages and limitations, which should always be taken into consideration when a survey is conducted for the best method to be selected. However, both techniques provide high quality point clouds that simulate the microtopography and texture to a high accuracy. The point cloud analysis comprises a defined XYZ value for every point, followed by an intensity value (due to the active source of the t-LiDAR method) or an RGB value (due to the passive source of the UAV method). This type of multi-vector analysis (sphere-by-sphere and point-by-point analysis) is currently a cutting-edge technology with significant potential in several geoscientific applications [119–122], while a combination of multi-source point clouds is feasible [123].

Current research denotes the utilization of combined multitemporal UAV images and Structure from Motion (SfM) technologies to systematically monitor both the topsoil

surface and volume change within small-scale watersheds [56,124]. In particular, recent studies [125–127] focus on point cloud analysis. As [108] indicated, the DEM cannot accurately represent the complex surface due to the 2D data used, while other researchers [128] highlight the efficiency of point cloud analysis in volumetric calculations. Point cloud analysis is a state-of-the-art technique, demonstrating an enhanced precision and a reduced occlusion within complex scenes featuring high roughness and topographic diversity across all dimensions [129]. Li et al. [130] denoted that the DoD technique results in a rapid and efficient computation, yet it may not be appropriate for analyzing significant surface changes in engineering buildings. The predominant method for change detection, the M3C2 algorithm, evaluates alterations along the local surface normal, which varies between points and overcomes the uncertainties associated with mesh or DEM generation. Three-dimensional point cloud analysis works directly with individual point cloud data, while DoD analysis includes gridded elevation data. Both methods have their strengths and limitations, and the selection between them depends on factors such as the nature of the data, the scale of the study area, and the specific objectives of the analysis. Integrating multiple data sources and employing complementary analysis techniques can help mitigate some of these limitations and improve the accuracy of surface change detection. Overall, this is the reason why the 3D point cloud analysis was selected. Yang et al. [131] provide spatial high-resolution monitoring of rill and inter-rill erosion development using t-LiDAR and SfM, achieving a fine resolution of 1 mm, as in our case, while Laburda et al. [132] employed SfM to capture splash erosion, reaching a resolution of 0.1 mm. A total GCP XYZ error less than 4 cm was reported by [56], as in our study area (total UAV–SfM error of 3 cm, Table 7).

Table 7. Resolution and total error estimation through the UAV–SfM analysis.

		Tiled Model (mm/pixel)	UAV Flight Height (m)	Total XYZ Error (cm)
Ilioupoli test site	8/2018	4	15	3
	3/2019	1	15	

The 3D modeling results presented in Table 7 highlight that the methodology proposed leads to a mm accuracy surface texture reconstruction and topsoil change detection. This value is clearly one order below the existing calculated error of 3 cm, which is already a sufficient error value for such applications. The combination of the technological tools leads to a detailed microtopography, reaching a resolution of 1 mm/px, a value significantly lower than the mechanical error of a t-LiDAR [46] or a GNSS receiver. There are applications where high-quality texture reconstruction is indeed needed, as in tracing paleoevents along fault planes through roughness studies for assessing fault slip rates or signal absorption-based surveys [133–135]. However, we have reached a milestone where no further detail is required, and technology is not a constraint on the soil erosion and sediment analyses. Similar t-LiDAR errors (a couple of cm) were also reported in [40,46].

GNSS technology was employed to monitor topsoil surface changes. Due to the challenging station surroundings, which involved obstructions, limited satellite coverage, and unfavorable geometric conditions, occasional disruptions in the GNSS signals, specialized data processing techniques for GNSS, were crucial in the dynamic deformation/change detection monitoring process. Many researchers have selected this methodology for its advances [65,136–140]. Zhang et al. [124] provided a comprehensive analysis of the suitability of commonly used centimeter-level UAV images and sub-meter-level Google Earth images for interpreting multi-dimensional morphological parameters of different gully morphologies based on GNSS RTK field measurements. In our test site, the ultimate goal was to provide high-accuracy data for comparison with the previous t-LiDAR- and UAV-collected data. This methodology was applied at the Ilioupoli test site and filled missing datasets due to vegetation growth. The GNSS error was 1 cm for the horizontal and 1.7 cm

for the vertical component. The combination of different technologies was proven accurate (offering cm accuracy) and necessary to complete the datasets (Table 6).

Extended research has been conducted in post-fire settings, due to the severe alteration on soil and vegetation/land-use. Runoff and the derived sediment yield volumes are significantly affected by the volume and intensity of precipitation, with the negative correlation with the vegetation cover decreasing in post-fire settings [141,142]. It is well established that high-severity wildfires reduce soil aggregate stability and enhance soil erodibility [143,144]. As a result, it should be highlighted that major flood events (as at the Ilioupoli test site) may also create an additional and severe topsoil disturbance. Recent research [145] demonstrated the increase in the mean annual erosion rates in 18 check dams (built in 2011), estimating 0.042 t/ha/year before the fire, 0.998 t/ha/year in the first 3 years after the fire, and 0.08 t/ha/year for the 20 years following the fire, by applying the WATEM/SEDEM erosion model and validated it through the retained sediment volumes of the dams.

Greek vegetation coverage is mostly constituted of flammable vegetation (such as pine trees and shrubs), leading to an environment highly susceptible to wildfire [146]. According to [13], the runoff rate increased three times and the soil loss was doubled after the forest fire in Spain. Previous research [17,18] showed that for the hillslope sediment yield balance, three to five years are usually required, while others [147] denoted the increase in sediment yield before and after the wildfire of 2009 in the Penteli region (Lykorrema watershed), where a mean pre-fire value of 0.02 t/ha/yr was replaced by a mean post-fire value of 0.13 t/ha/yr (for 2009–2014 estimation). The results displayed in this article are in agreement with previous researchers, showing that, in the Mediterranean conditions, the maximum soil erosion susceptibility is recorded within 4–6 months after the fire [148,149], as depicted in the Ilioupoli test site. Figures 11–15 highlight the importance of the sediment retention dams, since it was observed that, during the first intense rainfall events (65.6 mm of precipitation in September 2015), two months after the wildfire, 40 m³ of sediments are retained by the dam, while this volume decreased by 50% (20 m³) during the next 6-month assessment (October 2015 to April 2016), followed by an extra decrease of almost 90% (9 m³ in total of 2017–2020 assessment) during the next four years (if a mean value of 2.25 m³/yr is defined).

Overall, the final sediment measurements are demonstrated in Table 6 and in Figure 21 showing that these are in agreement with the theoretical background (with [150], Figure 21a). It is important to note that four independent methods were applied and all three of them provide results that are in close agreement to each other, adding confidence to the results.

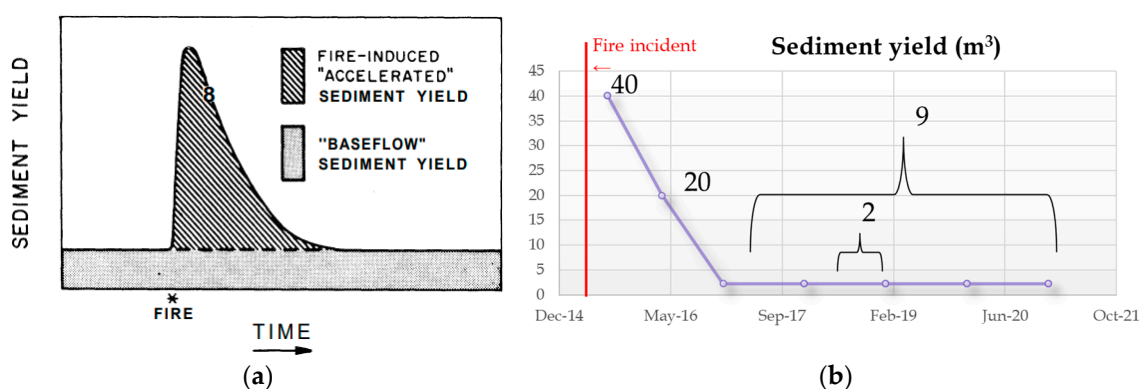


Figure 21. The post-fire sediment diagram according to [150] (a) applied to the Ilioupoli test site (b). Purple line indicates the sediment yield decrease.

5. Conclusions

This study introduces a methodological framework for monitoring and quantifying real-time soil erosion and sedimentation rates in post-fire settings. The methodology proposed includes UAV-SfM and t-LiDAR techniques that can be used as guidance for offering high-accuracy sediment yield deposition measurements based on the detailed analysis of

3D modeling and point cloud comparison. Concurrently, real-time monitoring data are feasibly leading to a multi-source point cloud comparison analysis at the multitemporal perspective, especially under the fast changing circumstances in relation to erosion, deposition, and vegetation growth in a Mediterranean wildfire-affected environment. Change detection quantification demands detailed measurements and process analysis. For this purpose, the point-to-point direct comparison and M3C2 distance algorithm performed well as an appropriate methodology to estimate soil erosion and calculate sedimentation volume. The UAV–SfM technique appears to accurately measure topsoil change detection and erosion/deposition patterns, and the derived point clouds adequately simulated the upland dam basin topsoil microtopography. Additionally, the point cloud analysis, when compiled with GNSS RTK surveys, can attain a centimeter resolution, obtaining reliable and accurate elevation data, when constraints appear. The GNSS analysis correlated to the t-LiDAR data, proving to be of great significance when long-term erosion rates and sedimentation volume calculations are required.

The combination of these technologies in soil erosion and sedimentation measurement was tested at the Ilioupoli test site (Athens, Greece) in order to measure the post-fire sedimentation rates following the severe wildfire event in 2015. This test site revealed that 40 m³ of sediment were deposited, following the first intense rainfall event, a value that was decreased by 50% during the next 6-month assessment, and continued to decrease further during the period of 2017–2021, validating the decrease in sediment yield deposition over the first years following a wildfire.

This research outlines that the UAV–SfM and t-LiDAR techniques offer high spatial resolution of a couple of millimeters per pixel and an accuracy of a couple of centimeters that clearly exceed our needs in the watershed scale. Considering also that they are cost-effective, non-invasive, and relatively fast methods, they should be regarded from now on as standard techniques for studying such processes. They address our need for flexibility in studying erosion dynamics even under the occurrence of individual significant rainfall events.

Overall, this study can serve as a reference guide and benchmark on high-accuracy sediment yield measurements, especially in mountainous catchments, providing an indirect estimate of erosion rates and offering a realistic assessment of a sediment retention dam's life expectancy. This is crucial for the prevention of flooding events and debris flows to nearby urban areas.

Author Contributions: Conceptualization, S.A. and I.P.; methodology, S.A. and I.P.; fieldwork, S.A. and S.S.; software, S.A.; validation, S.A. and I.P.; investigation, S.A.; resources, S.A. and K.R.; data curation, S.A.; GPR analysis, V.K.; writing—original draft preparation, S.A.; writing—review and editing, I.P. and K.R.; supervision, I.P. All authors have read and agreed to the published version of the manuscript.

Funding: This research is co-financed by Greece and the European Union (European Social Fund—ESF) through the Operational Program “Human Resources Development, Education and Lifelong Learning” in the context of the project “Strengthening Human Resources Research Potential via Doctorate Research—2nd Cycle” (MIS-5000432), implemented by the State Scholarships Foundation (IKY).



Data Availability Statement: The datasets presented in this article are not readily available because the data are part of an ongoing research.

Conflicts of Interest: The authors declare no conflicts of interest.

References

1. Dregne, H.E. Land Degradation in the Drylands. *Arid. Land Res. Manag.* **2002**, *16*, 99–132. [[CrossRef](#)]
2. Campo, J.; Andreu, V.; Gimeno-García, E.; González, O.; Rubio, J.L.; Campo, J.; Andreu, V.; Gimeno-García, E.; González, O.; Rubio, J.L. Occurrence of Soil Erosion after Repeated Experimental Fires in a Mediterranean Environment. *Geomorphology* **2006**, *82*, 376–387. [[CrossRef](#)]
3. Sougnez, N.; van Wesemael, B.; Vanacker, V. Low Erosion Rates Measured for Steep, Sparsely Vegetated Catchments in Southeast Spain. *CATENA* **2011**, *84*, 1–11. [[CrossRef](#)]
4. White, S.; Garcia-Ruiz, J. Extreme Erosional Events and Their Role in Mountain Areas of Northern Spain. *J. Hum. Environ.* **1998**, *27*, 300–305.
5. García-Ruiz, J.M.; Regüés, D.; Alvera, B.; Lana-Renault, N.; Serrano-Muela, P.; Nadal-Romero, E.; Navas, A.; Latron, J.; Martí-Bono, C.; Arnáez, J. Flood Generation and Sediment Transport in Experimental Catchments Affected by Land Use Changes in the Central Pyrenees. *J. Hydrol.* **2008**, *356*, 245–260. [[CrossRef](#)]
6. Montgomery, D.R.; Schmidt, K.M.; Greenberg, H.M.; Dietrich, W.E. Forest Clearing and Regional Landsliding. *Geology* **2000**, *28*, 311. [[CrossRef](#)]
7. Wilkinson, B.H.; McElroy, B.J. The Impact of Humans on Continental Erosion and Sedimentation. *GSA Bull.* **2007**, *119*, 140–156. [[CrossRef](#)]
8. Pausas, J.G. Changes in Fire and Climate in the Eastern Iberian Peninsula (Mediterranean Basin). *Clim. Chang.* **2004**, *63*, 337–350. [[CrossRef](#)]
9. Shakesby, R.A. Post-Wildfire Soil Erosion in the Mediterranean: Review and Future Research Directions. *Earth Sci. Rev.* **2011**, *105*, 71–100. [[CrossRef](#)]
10. Debano, L.F. The Effect of Fire on Soil Properties. In Proceedings of the Management and Productivity of Western-montane Forest Soils, Boise, ID, USA, 10–12 April 1990.
11. Certini, G. Effects of Fire on Properties of Forest Soils: A Review. *Oecologia* **2005**, *143*, 1–10. [[CrossRef](#)] [[PubMed](#)]
12. Wittenberg, L.; Inbar, M. The Role of Fire Disturbance on Runoff and Erosion Processes—A Long-Term Approach, Mt. Carmel Case Study, Israel. *Geogr. Res.* **2009**, *47*, 46–56. [[CrossRef](#)]
13. Inbar, M.; Tamir, M.; Wittenberg, L. Runoff and Erosion Processes after a Forest Fire in Mount Carmel, a Mediterranean Area. *Geomorphology* **1998**, *24*, 17–33. [[CrossRef](#)]
14. Whelan, R. The Ecology of Fire—Developments since 1995 and Outstanding Questions. *Proc. R. Soc. Qld.* **2009**, *115*, 59–68. [[CrossRef](#)]
15. Debano, L.F. The Role of Fire and Soil Heating on Water Repellency in Wildland Environments: A Review. *J. Hydrol.* **2000**, *231–232*, 195–206. [[CrossRef](#)]
16. Robichaud, P.R.; Waldrop, T.A. A Comparison of Surface Runoff and Sediment Yields from Low-Severity and High-Severity Site Preparation Burns. *Water Resour. Bull.* **1994**, *30*, 27–34. [[CrossRef](#)]
17. Benavides-Solorio, J.D.D.; MacDonald, L.H. Measurement and Prediction of Post-Fire Erosion at the Hillslope Scale, Colorado Front Range. *Int. J. Wildland Fire* **2005**, *14*, 457–474. [[CrossRef](#)]
18. Wagenbrenner, J.W.; MacDonald, L.H.; Rough, D. Effectiveness of Three Post-Fire Rehabilitation Treatments in the Colorado Front Range. *Hydrol. Process.* **2006**, *20*, 2989–3006. [[CrossRef](#)]
19. Poesen, J.; Nachtergaele, J.; Verstraeten, G.; Valentin, C. Gully Erosion and Environmental Change: Importance and Research Needs. *CATENA* **2003**, *50*, 91–133. [[CrossRef](#)]
20. Renard, K.; Foster, G.; Weessies, G.; McCool, D. Predicting Soil Erosion by Water: A Guide to Conservation Planning with the Revised Universal Soil Loss Equation (RUSLE). In *Agriculture Handbook 703*; Yoder, D.C., Ed.; U.S. Department of Agriculture: Washington, DC, USA, 1997.
21. Crosson, P. Will erosion threaten agricultural productivity? *Environ. Sci. Policy Sustain. Dev.* **1997**, *39*, 4–31. [[CrossRef](#)]
22. Poesen, J.W.A.; Hooke, J.M. Erosion, Flooding and Channel Management in Mediterranean Environments of Southern Europe. *Prog. Phys. Geogr.* **1997**, *21*, 157–199. [[CrossRef](#)]
23. Valero-Garcés, B.; Morellón, M.; Moreno, A.; Corella, J.P.; Martín-Puertas, C.; Barreiro, F.; Pérez, A.; Giral, S.; Mata-Campo, M.P. Lacustrine Carbonates of Iberian Karst Lakes: Sources, Processes and Depositional Environments. *Sediment. Geol.* **2014**, *299*, 1–29. [[CrossRef](#)]
24. Romero-Díaz, A.; Marín-Sanleandro, P.; Ortiz-Silla, R. Loss of Soil Fertility Estimated from Sediment Trapped in Check Dams. South-Eastern Spain. *CATENA* **2012**, *99*, 42–53. [[CrossRef](#)]
25. Verstraeten, G. Estimating Trap Efficiency of Small Reservoirs and Ponds: Methods and Implications for the Assessment of Sediment Yield. *Prog. Phys. Geogr.* **2000**, *24*, 219–251. [[CrossRef](#)]
26. Bazzoffi, P.; Baldassarre, G.; Vacca, S. Validation of PISA2 Model for Automatic Assessment of Reservoir Sedimentation. In *Proceedings of the International Conference on Reservoir Sedimentation*; Colorado State University: Fort Collins, CO, USA, 1996; pp. 519–528.
27. Lloyd, S.; Bishop, P.; Reinfelds, I. Shoreline Erosion: A Cautionary Note in Using Small Farm Dams to Determine Catchment Erosion Rates. *Earth Surf. Process. Landf. J. Br. Geomorphol. Group* **1998**, *23*, 905–912. [[CrossRef](#)]
28. Zhao, G.; Klik, A.; Mu, X.; Wang, F.; Gao, P.; Sun, W. Sediment Yield Estimation in a Small Watershed on the Northern Loess Plateau, China. *Geomorphology* **2015**, *241*, 343–352. [[CrossRef](#)]

29. Eltner, A.; Mulsow, C.; Maas, H.-G. Quantitative measurement of soil erosion from tls and uav data. *SPRS—Int. Arch. Photogramm. Remote Sens. Spat. Inf. Sci.* **2013**, *XL-1/W2*, 119–124. [[CrossRef](#)]
30. Li, Y.; Lu, X.; Washington-Allen, R.A.; Li, Y.; Ciampalini, A.; Li, Y.; Lu, X.; Washington-Allen, R.A.; Li, Y. Microtopographic Controls on Erosion and Deposition of a Rilled Hillslope in Eastern Tennessee, USA. *Remote Sens.* **2022**, *14*, 1315. [[CrossRef](#)]
31. Bolkas, D.; Naberezny, B.; Jacobson, M.G. Comparison of SUAS Photogrammetry and TLS for Detecting Changes in Soil Surface Elevations Following Deep Tillage. *J. Surv. Eng.* **2021**, *147*, 04021001. [[CrossRef](#)]
32. Vinci, A.; Brigante, R.; Todisco, F.; Mannocchi, F.; Radicioni, F. Measuring Rill Erosion by Laser Scanning. *CATENA* **2015**, *124*, 97–108. [[CrossRef](#)]
33. Sun, L.; Wu, S.; Zhang, B.; Lei, Q. Development of Rill Erosion and Its Simulation with Cellular Automata-Rill Model in Chinese Loess Plateau. *Arch. Agron. Soil Sci.* **2020**, *68*, 823–837. [[CrossRef](#)]
34. Lu, X.; Li, Y.; Washington-Allen, R.A.; Li, Y. Structural and Sedimentological Connectivity on a Rilled Hillslope. *Sci. Total Environ.* **2019**, *655*, 1479–1494. [[CrossRef](#)]
35. Li, Y.; McNelis, J.J.; Washington-Allen, R.A. Quantifying Short-Term Erosion and Deposition in an Active Gully Using Terrestrial Laser Scanning: A Case Study From West Tennessee, USA. *Front. Earth Sci.* **2020**, *8*, 587999. [[CrossRef](#)]
36. Perroy, R.L.; Bookhagen, B.; Asner, G.P.; Chadwick, O.A. Comparison of Gully Erosion Estimates Using Airborne and Ground-Based LiDAR on Santa Cruz Island, California. *Geomorphology* **2010**, *118*, 288–300. [[CrossRef](#)]
37. Rengers, F.K.; Tucker, G.E. The Evolution of Gully Headcut Morphology: A Case Study Using Terrestrial Laser Scanning and Hydrological Monitoring. *Earth Surf. Process Landf.* **2015**, *40*, 1304–1317. [[CrossRef](#)]
38. Castillo, C.; Pérez, R.; James, M.R.; Quinton, J.N.; Taguas, E.V.; Gómez, J.A. Comparing the Accuracy of Several Field Methods for Measuring Gully Erosion. *Soil Sci. Soc. Am. J.* **2012**, *76*, 1319–1332. [[CrossRef](#)]
39. Taylor, R.J.; Massey, C.; Fuller, I.C.; Marden, M.; Archibald, G.; Ries, W.; Taylor, R.J.; Massey, C.; Fuller, I.C.; Marden, M.; et al. Quantifying Sediment Connectivity in an Actively Eroding Gully Complex, Waipaoa Catchment, New Zealand. *Geomorphology* **2018**, *307*, 24–37. [[CrossRef](#)]
40. Domazetović, F.; Šiljeg, A.; Marić, I.; Panđa, L. A New Systematic Framework for Optimization of Multi-Temporal Terrestrial LiDAR Surveys over Complex Gully Morphology. *Remote Sens.* **2022**, *14*, 3366. [[CrossRef](#)]
41. Goodwin, N.R.; Armston, J.D.; Muir, J.; Stiller, I. Monitoring Gully Change: A Comparison of Airborne and Terrestrial Laser Scanning Using a Case Study from Aratula, Queensland. *Geomorphology* **2017**, *282*, 195–208. [[CrossRef](#)]
42. Magda Ramos, M.; Remondino, F. Data Fusion in Cultural Heritage—A Review. *Int. Arch. Photogramm. Remote Sens. Spat. Inf. Sci.—ISPRS Arch.* **2015**, *40*, 359–363. [[CrossRef](#)]
43. Xu, Z.; Wu, L.; Shen, Y.; Li, F.; Wang, Q.; Wang, R.; Lasaponara, R.; Masini, N.; Lorenzo, H.; Baghdadi, N.; et al. Tridimensional Reconstruction Applied to Cultural Heritage with the Use of Camera-Equipped UAV and Terrestrial Laser Scanner. *Remote Sens.* **2014**, *6*, 10413–10434. [[CrossRef](#)]
44. Su, Y.-T.; Bethel, J.; Hu, S. Octree-Based Segmentation for Terrestrial LiDAR Point Cloud Data in Industrial Applications. *ISPRS J. Photogramm. Remote Sens.* **2016**, *113*, 59–74. [[CrossRef](#)]
45. Barba, S.; Barbarella, M.; Di Benedetto, A.; Fiani, M.; Gujski, L.; Limongiello, M. Accuracy Assessment of 3D Photogrammetric Models from an Unmanned Aerial Vehicle. *Drones* **2019**, *3*, 79. [[CrossRef](#)]
46. Alexiou, S.; Deligiannakis, G.; Pallikarakis, A.; Papanikolaou, I.; Psomiadis, E.; Reicherter, K. Comparing High Accuracy T-Lidar and Uav-Sfm Derived Point Clouds for Geomorphological Change Detection. *ISPRS Int. J. Geoinf.* **2021**, *10*, 367. [[CrossRef](#)]
47. Alexiou, S.; Efthimiou, N.; Karamesouti, M.; Papanikolaou, I.; Psomiadis, E.; Charizopoulos, N. Measuring Annual Sedimentation through High Accuracy UAV-Photogrammetry Data and Comparison with RUSLE and PESERA Erosion Models. *Remote Sens.* **2023**, *15*, 1339. [[CrossRef](#)]
48. Bird, S.; Hogan, D.; Schwab, J. Photogrammetric Monitoring of Small Streams under a Riparian Forest Canopy. *Earth Surf. Process Landf.* **2010**, *35*, 952–970. [[CrossRef](#)]
49. Lane, S.N.; James, T.D.; Crowell, M.D. Application of Digital Photogrammetry to Complex Topography for Geomorphological Research. *Photogramm. Rec.* **2000**, *16*, 793–821. [[CrossRef](#)]
50. Chandler, J.; Ashmore, P.; Paola, C.; Gooch, M.; Varkaris, F. Monitoring River-Channel Change Using Terrestrial Oblique Digital Imagery and Automated Digital Photogrammetry. *Ann. Assoc. Am. Geogr.* **2002**, *92*, 631–644. [[CrossRef](#)]
51. Brasington, J.; Smart, R.M.A. Close Range Digital Photogrammetric Analysis of Experimental Drainage Basin Evolution. *Earth Surf. Process Landf.* **2003**, *28*, 231–247. [[CrossRef](#)]
52. Barker, R.; Dixon, L.; Hooke, J. Use of Terrestrial Photogrammetry for Monitoring and Measuring Bank Erosion. *Earth Surf. Process Landf.* **1997**, *22*, 1217–1227. [[CrossRef](#)]
53. Pyle, C.J.; Richards, K.S.; Chandler, J.H. Digital Photogrammetric Monitoring of River Bank Erosion. *Photogramm. Rec.* **1997**, *15*, 753–764. [[CrossRef](#)]
54. Marzolf, I.; Poesen, J. The Potential of 3D Gully Monitoring with GIS Using High-Resolution Aerial Photography and a Digital Photogrammetry System. *Geomorphology* **2009**, *111*, 48–60. [[CrossRef](#)]
55. Betts, H.D.; DeRose, R.C. Digital Elevation Models as a Tool for Monitoring and Measuring Gully Erosion. *Int. J. Appl. Earth Obs. Geoinf.* **1999**, *1*, 91–101. [[CrossRef](#)]
56. Wang, R.; Sun, H.; Yang, J.; Zhang, S.; Fu, H.; Wang, N.; Liu, Q. Quantitative Evaluation of Gully Erosion Using Multitemporal UAV Data in the Southern Black Soil Region of Northeast China: A Case Study. *Remote Sens.* **2022**, *14*, 1479. [[CrossRef](#)]

57. Cândido, B.M.; Quinton, J.N.; James, M.R.; Silva, M.L.N.; de Carvalho, T.S.; de Lima, W.; Beniaich, A.; Eltner, A. High-Resolution Monitoring of Diffuse (Sheet or Interrill) Erosion Using Structure-from-Motion. *Geoderma* **2020**, *375*, 114477. [[CrossRef](#)]
58. Rossi, G.; Luca Tanteri, I.; Tofani, V.; Vannocci, P.; Moretti, S.; Casagli, N. Multitemporal UAV Surveys for Landslide Mapping and Characterization. *Landslides* **2018**, *15*, 1045–1052. [[CrossRef](#)]
59. D'Oleire-Oltmanns, S.; Marzolf, I.; Peter, K.D.; Ries, J.B. Unmanned Aerial Vehicle (UAV) for Monitoring Soil Erosion in Morocco. *Remote Sens.* **2012**, *4*, 3390–3416. [[CrossRef](#)]
60. Hamshaw, S.D.; Engel, T.; Rizzo, D.M.; O'Neil-Dunne, J.; Dewoolkar, M.M. Application of Unmanned Aircraft System (UAS) for Monitoring Bank Erosion along River Corridors. *Geomat. Nat. Hazards Risk* **2019**, *10*, 1285–1305. [[CrossRef](#)]
61. Hayakawa, Y.S.; Obanawa, H. Volumetric Change Detection in Bedrock Coastal Cliffs Using Terrestrial Laser Scanning and UAS-Based SfM. *Sensors* **2020**, *20*, 3403. [[CrossRef](#)] [[PubMed](#)]
62. Neugirg, F.; Kaiser, A.; Huber, A.; Heckmann, T.; Schindewolf, M.; Schmidt, J.; Becht, M.; Haas, F. Using Terrestrial LiDAR Data to Analyse Morphodynamics on Steep Unvegetated Slopes Driven by Different Geomorphic Processes. *CATENA* **2016**, *142*, 269–280. [[CrossRef](#)]
63. Kim, J.; Kim, I.; Ha, E.; Choi, B. UAV Photogrammetry for Soil Surface Deformation Detection in a Timber Harvesting Area, South Korea. *Forests* **2023**, *14*, 980. [[CrossRef](#)]
64. Deligiannakis, G.; Pallikarakis, A.; Papanikolaou, I.; Alexiou, S.; Reicherter, K. Detecting and Monitoring Early Post-Fire Sliding Phenomena Using Uav-Sfm Photogrammetry and t-Lidar-Derived Point Clouds. *Fire* **2021**, *4*, 87. [[CrossRef](#)]
65. Mavroulis, S.; Vassilakis, E.; Diakakis, M.; Konsolaki, A.; Kaviris, G.; Kotsi, E.; Kapetanidis, V.; Sakkas, V.; Alexopoulos, J.D.; Lekkas, E.; et al. The Use of Innovative Techniques for Management of High-Risk Coastal Areas, Mitigation of Earthquake-Triggered Landslide Risk and Responsible Coastal Development. *Appl. Sci.* **2022**, *12*, 2193. [[CrossRef](#)]
66. Haneberg, W.C. Using Close Range Terrestrial Digital Photogrammetry for 3-D Rock Slope Modeling and Discontinuity Mapping in the United States. *Bull. Eng. Geol. Environ.* **2008**, *67*, 457–469. [[CrossRef](#)]
67. Castellazzi, G.; D'Altri, A.M.; Bitelli, G.; Selvaggi, I.; Lambertini, A. From Laser Scanning to Finite Element Analysis of Complex Buildings by Using a Semi-Automatic Procedure. *Sensors* **2015**, *15*, 18360–18380. [[CrossRef](#)]
68. Jaboyedoff, M.; Oppikofer, T.; Abellán, A.; Derron, M.H.; Loye, A.; Metzger, R.; Pedrazzini, A. Use of LIDAR in Landslide Investigations: A Review. *Nat. Hazards* **2012**, *61*, 5–28. [[CrossRef](#)]
69. Abellán, A.; Oppikofer, T.; Jaboyedoff, M.; Rosser, N.J.; Lim, M.; Lato, M.J. Terrestrial Laser Scanning of Rock Slope Instabilities. *Earth Surf. Process Landf.* **2014**, *39*, 80–97. [[CrossRef](#)]
70. Eltner, A.; Schneider, D. Analysis of Different Methods for 3D Reconstruction of Natural Surfaces from Parallel-Axes UAV Images. *Photogramm. Rec.* **2015**, *30*, 279–299. [[CrossRef](#)]
71. Anderson, K.; Westoby, M.J.; James, M.R. Low-Budget Topographic Surveying Comes of Age: Structure from Motion Photogrammetry in Geography and the Geosciences. *Prog. Phys. Geogr.* **2019**, *43*, 163–173. [[CrossRef](#)]
72. Blanch, X.; Eltner, A.; Guinau, M.; Abellan, A. Multi-Epoch and Multi-Imagery (MEMI) Photogrammetric Workflow for Enhanced Change Detection Using Time-Lapse Cameras. *Remote Sens.* **2021**, *13*, 1460. [[CrossRef](#)]
73. Vassilakis, E.; Konsolaki, A.; Petrakis, S.; Kotsi, E.; Fillis, C.; Lozios, S.; Lekkas, E. 4D Point Cloud Analysis of the September 2020 Medicane Impact on Myrtos Beach in Cephalonia, Greece. In Proceedings of the 5th Joint International Symposium on Deformation Monitoring (JISDM), Valencia, Spain, 20–22 June 2022.
74. Castagnetti, C.; Bertacchini, E.; Corsini, A.; Rivola, R. A Reliable Methodology for Monitoring Unstable Slopes: The Multi-Platform and Multi-Sensor Approach. In Proceedings of the SPIE, Earth Resources and Environmental Remote Sensing/GIS Applications V, Amsterdam, The Netherlands, 23–25 September 2014; Volume 9245, p. 92450J. [[CrossRef](#)]
75. Kyriou, A.; Nikolakopoulos, K.; Koukouvelas, I.; Lampropoulou, P. Repeated UAV Campaigns, GNSS Measurements, GIS, and Petrographic Analyses for Landslide Mapping and Monitoring. *Minerals* **2021**, *11*, 300. [[CrossRef](#)]
76. Gili, J.A.; Corominas, J.; Rius, J. Using Global Positioning System Techniques in Landslide Monitoring. *Eng. Geol.* **2000**, *55*, 167–192. [[CrossRef](#)]
77. Mantovani, M.; Bossi, G.; Dykes, A.P.; Pasuto, A.; Soldati, M.; Devoto, S. Coupling Long-Term GNSS Monitoring and Numerical Modelling of Lateral Spreading for Hazard Assessment Purposes. *Eng. Geol.* **2022**, *296*, 106466. [[CrossRef](#)]
78. Nikolakopoulos, K.; Kavoura, K.; Depountis, N.; Kyriou, A.; Argyropoulos, N.; Koukouvelas, I.; Sabatakakis, N. Preliminary Results from Active Landslide Monitoring Using Multidisciplinary Surveys. *Eur. J. Remote Sens.* **2017**, *50*, 280–299. [[CrossRef](#)]
79. Lague, D.; Brodu, N.; Leroux, J. Accurate 3D Comparison of Complex Topography with Terrestrial Laser Scanner: Application to the Rangitikei Canyon (N-Z). *ISPRS J. Photogramm. Remote Sens.* **2013**, *82*, 10–26. [[CrossRef](#)]
80. Kharroubi, A.; Poux, F.; Ballouch, Z.; Hajji, R.; Billen, R. Three Dimensional Change Detection Using Point Clouds: A Review. *Geomatics* **2022**, *2*, 457–485. [[CrossRef](#)]
81. Roşca, S.; Suomalainen, J.; Bartholomeus, H.; Herold, M. Comparing Terrestrial Laser Scanning and Unmanned Aerial Vehicle Structure from Motion to Assess Top of Canopy Structure in Tropical Forests. *Interface Focus*. **2018**, *8*, 20170038. [[CrossRef](#)]
82. Stumpf, A.; Malet, J.P.; Allemand, P.; Pierrot-Deseilligny, M.; Skupinski, G. Ground-Based Multi-View Photogrammetry for the Monitoring of Landslide Deformation and Erosion. *Geomorphology* **2015**, *231*, 130–145. [[CrossRef](#)]
83. Cao, L.; Liu, H.; Fu, X.; Zhang, Z.; Shen, X.; Ruan, H. Comparison of UAV LiDAR and Digital Aerial Photogrammetry Point Clouds for Estimating Forest Structural Attributes in Subtropical Planted Forests. *Forests* **2019**, *10*, 145. [[CrossRef](#)]

84. Wheaton, J.M.; Brasington, J.; Darby, S.E.; Sear, D.A. Accounting for Uncertainty in DEMs from Repeat Topographic Surveys: Improved Sediment Budgets. *Earth Surf. Process Landf.* **2010**, *35*, 136–156. [[CrossRef](#)]
85. Williams, R. DEMs of Difference. *Geomorphol. Tech.* **2012**, *2*, 1–17.
86. Okyay, U.; Telling, J.; Glennie, C.L.; Dietrich, W.E. Airborne Lidar Change Detection: An Overview of Earth Sciences Applications. *Earth Sci. Rev.* **2019**, *198*, 102929. [[CrossRef](#)]
87. Kakavas, M.P.; Nikolakopoulos, K.G.; Havenith, H.-B.; Martinez-Frias, J. Digital Elevation Models of Rockfalls and Landslides: A Review and Meta-Analysis. *Geosciences* **2021**, *11*, 256. [[CrossRef](#)]
88. Lissak, C.; Bartsch, A.; De Michele, M.; Gomez, C.; Maquaire, O.; Raucoules, D.; Roulland, T. Remote Sensing for Assessing Landslides and Associated Hazards. *Surv. Geophys.* **2020**, *41*, 1391–1435. [[CrossRef](#)]
89. Abellan, A.; Derron, M.-H.; Jaboyedoff, M.; Derron@unil, M.-H.; Ch, M.-H.D.; Ch, M.J. “Use of 3D Point Clouds in Geohazards” Special Issue: Current Challenges and Future Trends. *Remote Sens.* **2016**, *8*, 130. [[CrossRef](#)]
90. Parenti, C.; Rossi, P.; Mancini, F.; Scorpio, V.; Grassi, F.; Ciccarese, G.; Lugli, F.; Soldati, M. Multitemporal Analysis of Slow-Moving Landslides and Channel Dynamics through Integrated Remote Sensing and In Situ Techniques. *Remote Sens.* **2023**, *15*, 3563. [[CrossRef](#)]
91. Arza-García, M.; Gonçalves, J.A.; Ferreira Pinto, V.; Bastos, G. On-Site Stability Assessment of Rubble Mound Breakwaters Using Unmanned Aerial Vehicle-Based Photogrammetry and Random Sample Consensus. *Remote Sens.* **2024**, *16*, 331. [[CrossRef](#)]
92. Keeley, J.E.; Keeley, J.E. Fire Intensity, Fire Severity and Burn Severity: A Brief Review and Suggested Usage. *Int. J. Wildland Fire* **2009**, *18*, 116–126. [[CrossRef](#)]
93. Chen, X.; Vogelmann, J.E.; Rollins, M.; Ohlen, D.; Key, C.H.; Yang, L.; Huang, C.; Shi, H. Detecting Post-Fire Burn Severity and Vegetation Recovery Using Multitemporal Remote Sensing Spectral Indices and Field-Collected Composite Burn Index Data in a Ponderosa Pine Forest. *Int. J. Remote Sens.* **2011**, *32*, 7905–7927. [[CrossRef](#)]
94. Ireland, G.; Petropoulos, G.P. Exploring the Relationships between Post-Fire Vegetation Regeneration Dynamics, Topography and Burn Severity: A Case Study from the Montane Cordillera Ecozones of Western Canada. *Appl. Geogr.* **2015**, *56*, 232–248. [[CrossRef](#)]
95. Mallinis, G.; Mitsopoulos, I.; Chrysafi, I. Evaluating and Comparing Sentinel 2A and Landsat-8 Operational Land Imager (OLI) Spectral Indices for Estimating Fire Severity in a Mediterranean Pine Ecosystem of Greece. *GIScience Remote Sens.* **2017**, *55*, 1–18. [[CrossRef](#)]
96. Papanikolaou, D.I. *The Geology of Greece*; Springer International Publishing: Cham, Switzerland, 2021; ISBN 978-3-030-60730-2.
97. Latsoudas Ch. Geological Map “Koropi-Plaka”, 1:50,000; eagme.gr: 2003.
98. Kehrle, V.C. *Erosional Consequences of Forest Fires in Attica Region (Central Greece)—Using GPR to Validate Erosion Rates from Check Dam Infill*; RWTH: Aachen, Germany, 2016.
99. Conyers, L.B. *Ground Penetrating Radar for Archaeology*; Altamira Press: Lanham, MD, USA, 2004.
100. Neal, A. Ground-Penetrating Radar and Its Use in Sedimentology: Principles, Problems and Progress. *Earth Sci. Rev.* **2004**, *66*, 261–330. [[CrossRef](#)]
101. Jaud, M.; Passot, S.; Allemand, P.; Le Dantec, N.; Grandjean, P.; Delacourt, C. Suggestions to Limit Geometric Distortions in the Reconstruction of Linear Coastal Landforms by SfM Photogrammetry with PhotoScan® and MicMac® for UAV Surveys with Restricted GCPs Pattern. *Drones* **2018**, *3*, 2. [[CrossRef](#)]
102. Taddia, Y.; Corbau, C.; Zambello, E.; Pellegrinelli, A. UAVs for Structure-from-Motion Coastal Monitoring: A Case Study to Assess the Evolution of Embryo Dunes over a Two-Year Time Frame in the Po River Delta, Italy. *Sensors* **2019**, *19*, 1717. [[CrossRef](#)] [[PubMed](#)]
103. Can, M.; Çalıřır, E.; Akpınar, A. Spatio-Temporal Changes in Downstream River Bed during a Dam Construction. *KSCE J. Civ. Eng.* **2022**, *26*, 2160–2173. [[CrossRef](#)]
104. Gelagay, H.S.; Minale, A.S. Soil Loss Estimation Using GIS and Remote Sensing Techniques: A Case of Koga Watershed, Northwestern Ethiopia. *Int. Soil Water Conserv. Res.* **2016**, *4*, 126–136. [[CrossRef](#)]
105. Kayet, N.; Pathak, K.; Chakrabarty, A.; Sahoo, S. Evaluation of Soil Loss Estimation Using the RUSLE Model and SCS-CN Method in Hillslope Mining Areas. *Int. Soil Water Conserv. Res.* **2018**, *6*, 31–42. [[CrossRef](#)]
106. Lu, X.; Li, Y.; Washington-Allen, R.A.; Li, Y.; Li, H.; Hu, Q. The Effect of Grid Size on the Quantification of Erosion, Deposition, and Rill Network. *Int. Soil Water Conserv. Res.* **2017**, *5*, 241–251. [[CrossRef](#)]
107. Dai, W.; Yang, X.; Na, J.; Li, J.; Brus, D.; Xiong, L.; Tang, G.; Huang, X. Effects of DEM Resolution on the Accuracy of Gully Maps in Loess Hilly Areas. *CATENA* **2019**, *177*, 114–125. [[CrossRef](#)]
108. Monserrat, O.; Crosetto, M. Deformation Measurement Using Terrestrial Laser Scanning Data and Least Squares 3D Surface Matching. *ISPRS J. Photogramm. Remote Sens.* **2008**, *63*, 142–154. [[CrossRef](#)]
109. Sepuru, T.; Dube, T. An appraisal on the progress of remote sensing applications in soil erosion mapping and monitoring. *Remote Sens. Appl. Soc. Environ.* **2018**, *9*, 1–9. [[CrossRef](#)]
110. LI, Y.; Bai, X.; Tian, Y.; Luo, G. Review and Future Research Directions about Major Monitoring Method of Soil Erosion. *IOP Conf. Ser. Earth Env. Sci.* **2017**, *63*, 012042. [[CrossRef](#)]
111. Xie, F.; Zhao, G.; Mu, X.; Tian, P.; Gao, P.; Sun, W. Sediment Yield in Dam-Controlled Watersheds in the Pisha Sandstone Region on the Northern Loess Plateau, China. *Land* **2021**, *10*, 1264. [[CrossRef](#)]
112. McGregor, D. *Desertification: Exploding the Myth*, D.S.G. Thomas and N. J. Middleton. Wiley, Chichester, 1994. ISBN 0 471 94815 2, £32.50 (Hardback), Xiii + 194 Pp. *Land Degrad. Dev.* **1995**, *6*, 69–70. [[CrossRef](#)]

113. Scott, D.; Versfeld, D.B.; Lesch, W. Erosion and Sediment Yield in Relation to Afforestation and Fire in the Mountains of the Western Cape Province, South Africa. *S. Afr. Geogr. J.* **1998**, *80*, 52–59. [[CrossRef](#)]
114. García-Comendador, J.; Martínez-Carreras, N.; Fortesa, J.; Borràs, A.; Calsamiglia, A.; Estrany, J. Analysis of Post-Fire Suspended Sediment Sources by Using Colour Parameters. *Geoderma* **2020**, *379*, 114638. [[CrossRef](#)]
115. Panagos, P.; Borrelli, P.; Meusburger, K.; Alewell, C.; Lugato, E.; Montanarella, L. Estimating the Soil Erosion Cover-Management Factor at the European Scale. *Land Use Policy* **2015**, *48*, 38–50. [[CrossRef](#)]
116. González-Romero, J.; López-Vicente, M.; Gómez-Sánchez, E.; Peña-Molina, E.; Galletero, P.; Plaza-Álvarez, P.; Fajardo-Cantos, A.; Moya, D.; De las Heras, J.; Lucas-Borja, M.E. Post-Fire Management Effects on Hillslope-Stream Sediment Connectivity in a Mediterranean Forest Ecosystem. *J. Environ. Manag.* **2022**, *316*, 115212. [[CrossRef](#)] [[PubMed](#)]
117. Ward, M.; Southwell, D.; Gallagher, R.V.; Raadik, T.A.; Whiterod, N.S.; Lintermans, M.; Sheridan, G.; Nyman, P.; Suárez-Castro, A.F.; Marsh, J.; et al. Modelling the Spatial Extent of Post-Fire Sedimentation Threat to Estimate the Impacts of Fire on Waterways and Aquatic Species. *Divers. Distrib.* **2022**, *28*, 2429–2442. [[CrossRef](#)]
118. Castillo, C.; Gómez, J.A. A Century of Gully Erosion Research: Urgency, Complexity and Study Approaches. *Earth Sci. Rev.* **2016**, *160*, 300–319. [[CrossRef](#)]
119. Andaru, R.; Cahyono, B.K.; Riyadi, G.; Istarno; Djurdjani; Ramadhan, G.R.; Tuntas, S. The Combination of Terrestrial Lidar and UAV Photogrammetry for Interactive Architectural Heritage Visualization Using Unity 3D Game Engine. *Int. Arch. Photogramm. Remote Sens. Spat. Inf. Sci.—ISPRS Arch.* **2019**, *42*, 39–44. [[CrossRef](#)]
120. Mayr, A.; Rutzinger, M.; Bremer, M.; Oude Elberink, S.; Stumpf, F.; Geitner, C. Object-based classification of terrestrial laser scanning point clouds for landslide monitoring. *Photogram. Rec.* **2017**, *32*, 377–397. [[CrossRef](#)]
121. Turner, D.; Lucieer, A.; Watson, C. An Automated Technique for Generating Georectified Mosaics from Ultra-High Resolution Unmanned Aerial Vehicle (UAV) Imagery, Based on Structure from Motion (SfM) Point Clouds. *Remote Sens.* **2012**, *4*, 1392–1410. [[CrossRef](#)]
122. Woodget, A.S.; Austrums, R. Subaerial Gravel Size Measurement Using Topographic Data Derived from a UAV-SfM Approach. *Earth Surf. Process Landf.* **2017**, *42*, 1434–1443. [[CrossRef](#)]
123. Vassilakis, E.; Konsolaki, A. Quantification of Cave Geomorphological Characteristics Based on Multi Source Point Cloud Data Interoperability. *Z. Fur Geomorphol.* **2022**, *63*, 265–277. [[CrossRef](#)]
124. Zhang, C.; Wang, C.; Long, Y.; Pang, G.; Shen, H.; Wang, L.; Yang, Q. Comparative Analysis of Gully Morphology Extraction Suitability Using Unmanned Aerial Vehicle and Google Earth Imagery. *Remote Sens.* **2023**, *15*, 4302. [[CrossRef](#)]
125. Kermarrec, G.; Yang, Z.; Czerwonka-Schröder, D. Classification of Terrestrial Laser Scanner Point Clouds: A Comparison of Methods for Landslide Monitoring from Mathematical Surface Approximation. *Remote Sens.* **2022**, *14*, 5099. [[CrossRef](#)]
126. Anders, K.; Winiwarter, L.; Mara, H.; Lindenbergh, R.; Vos, S.E.; Höfle, B. Fully Automatic Spatiotemporal Segmentation of 3D LiDAR Time Series for the Extraction of Natural Surface Changes. *ISPRS J. Photogramm. Remote Sens.* **2021**, *173*, 297–308. [[CrossRef](#)]
127. Huang, R.; Jiang, L.; Shen, X.; Dong, Z.; Zhou, Q.; Yang, B.; Wang, H. An Efficient Method of Monitoring Slow-Moving Landslides with Long-Range Terrestrial Laser Scanning: A Case Study of the Dashu Landslide in the Three Gorges Reservoir Region, China. *Landslides* **2019**, *16*, 839–855. [[CrossRef](#)]
128. Nourbakhshbeidokhti, S.; Kinoshita, A.M.; Chin, A.; Florsheim, J.L. A Workflow to Estimate Topographic and Volumetric Changes and Errors in Channel Sedimentation after Disturbance. *Remote Sens.* **2019**, *11*, 586. [[CrossRef](#)]
129. Williams, J.G.; Anders, K.; Winiwarter, L.; Zahs, V.; Höfle, B. Multi-Directional Change Detection between Point Clouds. *ISPRS J. Photogramm. Remote Sens.* **2021**, *172*, 95–113. [[CrossRef](#)]
130. Li, Y.; Liu, P.; Li, H.; Huang, F.; Li, Y.; Liu, P.; Li, H.; Huang, F. A Comparison Method for 3D Laser Point Clouds in Displacement Change Detection for Arch Dams. *ISPRS Int. J. Geo-Inf.* **2021**, *10*, 184. [[CrossRef](#)]
131. Yang, Y.; Shi, Y.; Liang, X.; Huang, T.; Fu, S.; Liu, B. Evaluation of Structure from Motion (SfM) Photogrammetry on the Measurement of Rill and Interrill Erosion in a Typical Loess. *Geomorphology* **2021**, *385*, 107734. [[CrossRef](#)]
132. Laburda, T.; Krása, J.; Zúmr, D.; Devátý, J.; Vrána, M.; Zambon, N.; Johannsen, L.L.; Klik, A.; Strauss, P.; Dostál, T. SfM-MVS Photogrammetry for Splash Erosion Monitoring under Natural Rainfall. *Earth Surf. Process Landf.* **2021**, *46*, 1067–1082. [[CrossRef](#)]
133. Schneiderwind, S.; Mason, J.; Wiatr, T.; Papanikolaou, I.; Reicherter, K. 3-D Visualisation of Palaeoseismic Trench Stratigraphy and Trench Logging Using Terrestrial Remote Sensing and GPR – A Multiparametric Interpretation. *Solid Earth* **2016**, *7*, 323–340. [[CrossRef](#)]
134. Mason, J.; Schneiderwind, S.; Wiatr, T.; Reicherter, K.; Pallikarakis, A.; Papanikolaou, I.; Mechernich, S.; Wiatr, T. Fault Structure and Deformation Rates at the Lastros-Sfaka Graben, Crete. *Tectonophysics* **2016**, *683*, 216–232. [[CrossRef](#)]
135. Wiatr, T.; Papanikolaou, I.; Fernández-Steeger, T.; Reicherter, K. Bedrock Fault Scarp History: Insight from t-LiDAR Backscatter Behaviour and Analysis of Structure Changes. *Geomorphology* **2015**, *228*, 421–431. [[CrossRef](#)]
136. Zhou, X.; Zhang, S.; Zhang, Q.; Liu, Q.; Ma, Z.; Wang, T.; Tian, J.; Li, X. Research of Deformation and Soil Moisture in Loess Landslide Simultaneous Retrieved with Ground-Based GNSS. *Remote Sens.* **2022**, *14*, 5687. [[CrossRef](#)]
137. Carlà, T.; Tofani, V.; Lombardi, L.; Raspini, F.; Bianchini, S.; Bertolo, D.; Thuegaz, P.; Casagli, N. Combination of GNSS, Satellite InSAR, and GBInSAR Remote Sensing Monitoring to Improve the Understanding of a Large Landslide in High Alpine Environment. *Geomorphology* **2019**, *335*, 62–75. [[CrossRef](#)]

138. Calcaterra, S.; Cesi, C.; Di Maio, C.; Gambino, P.; Merli, K.; Vallario, M.; Vassallo, R. Surface Displacements of Two Landslides Evaluated by GPS and Inclinometer Systems: A Case Study in Southern Apennines, Italy. *Nat. Hazards* **2012**, *61*, 257–266. [[CrossRef](#)]
139. Huang, G.; Du, S.; Wang, D. GNSS techniques for real-time monitoring of landslides: A review. *Satell. Navig.* **2023**, *4*, 5. [[CrossRef](#)]
140. Pineux, N.; Lisein, J.; Swerts, G.; Bielders, C.L.; Lejeune, P.; Colinet, G.; Degré, A. Can DEM Time Series Produced by UAV Be Used to Quantify Diffuse Erosion in an Agricultural Watershed? *Geomorphology* **2017**, *280*, 122–136. [[CrossRef](#)]
141. Barreiro-Lostres, F.; Moreno, A.; González-Sampériz, P.; Giral, S.; Nadal-Romero, E.; Valero-Garcés, B. Erosion in Mediterranean Mountain Landscapes during the Last Millennium: A Quantitative Approach Based on Lake Sediment Sequences (Iberian Range, Spain). *CATENA* **2017**, *149*, 782–798. [[CrossRef](#)]
142. García-Ruiz, J.M.; Beguería, S.; Nadal-Romero, E.; González-Hidalgo, J.C.; Lana-Renault, N.; Sanjuán, Y. A Meta-Analysis of Soil Erosion Rates across the World. *Geomorphology* **2015**, *239*, 160–173. [[CrossRef](#)]
143. Cerda, A.; Imeson, A.C.; Calvo, A. Fire and Aspect Induced Differences on the Erodibility and Hydrology of Soils at La Costera, Valencia, Southeast Spain. *CATENA* **1995**, *24*, 289–304. [[CrossRef](#)]
144. Mataix-Solera, J.; Doerr, S.H.; Mataix-Solera, J.; Doerr, S.H. Hydrophobicity and Aggregate Stability in Calcareous Topsoils from Fire-Affected Pine Forests in Southeastern Spain. *Geode* **2004**, *118*, 77–88. [[CrossRef](#)]
145. Margiorou, S.; Kastridis, A.; Sapountzis, M. Pre/Post-Fire Soil Erosion and Evaluation of Check-Dams Effectiveness in Mediterranean Suburban Catchments Based on Field Measurements and Modeling. *Land* **2022**, *11*, 1705. [[CrossRef](#)]
146. Kozłowski, T.T. Fire and Ecosystems. Kozłowski, T.T., Ahlgren, C.E., Eds.; 1974. Available online: https://books.google.gr/books/about/Fire_and_Ecosystems.html?id=gNRY4rmVq_kC&redir_esc=y (accessed on 19 January 2024).
147. Soulis, K.X.; Generali, K.A.; Papadaki, C.; Theodoropoulos, C.; Psomiadis, E. Hydrological Response of Natural Mediterranean Watersheds to Forest Fires. *Hydrology* **2021**, *8*, 15. [[CrossRef](#)]
148. Sala; Soler, M.; Pradas, M. Temporal and Spatial Variations in Runoff and Erosion in Burnt Soils. In Proceedings of the 2nd International Conference Forest Fire Research, Comissão de Coordenação Da Região Centro, Coimbra, Portugal, 21–24 November 1994; pp. 1123–1134.
149. Andreu, V.; Imeson, A.C.; Rubio, J.L. Temporal Changes in Soil Aggregates and Water Erosion after a Wildfire in a Mediterranean Pine Forest. *CATENA* **2001**, *44*, 69–84. [[CrossRef](#)]
150. Swanson, F.J. Fire and Geomorphic Processes. In Proceedings of the Fire Regimed and Ecosystems Conference, Honolulu, HI, USA, 11–15 December 1978.

Disclaimer/Publisher’s Note: The statements, opinions and data contained in all publications are solely those of the individual author(s) and contributor(s) and not of MDPI and/or the editor(s). MDPI and/or the editor(s) disclaim responsibility for any injury to people or property resulting from any ideas, methods, instructions or products referred to in the content.